

# Optical and X-ray properties of the RIXOS AGN: II - Emission lines

E. M. Puchnarewicz,<sup>1</sup> K. O. Mason,<sup>1</sup> F. J. Carrera,<sup>1,2</sup> W. N. Brandt,<sup>3,4</sup>  
 F. Cabrera-Guera,<sup>5</sup> R. Carballo,<sup>6,7</sup> G. Hasinger,<sup>8</sup> R. G. McMahon,<sup>3</sup>  
 J. P. D. Mittaz,<sup>1</sup> M. J. Page,<sup>1</sup> I. Perez-Fournon,<sup>5</sup> and A. Schwone<sup>8</sup>

<sup>1</sup> Mullard Space Science Laboratory, University College London, Holmbury St. Mary, Dorking, Surrey RH5 6NT, UK.  
<sup>2</sup> Present address: Instituto de Física de Cantabria CSIC-UC, Facultad de Ciencias, Avda. de los Castros s/n 39005, Santander, Spain.

<sup>3</sup> Institute of Astronomy, Madingley Road, Cambridge CB3 0HA, UK.

<sup>4</sup> Present address: Harvard-Smithsonian Center for Astrophysics, 60 Garden Street, Cambridge, MA 02138, USA

<sup>5</sup> Instituto de Astrofísica de Canarias Vía Láctea s/n 38200 La Laguna, Tenerife, Spain

<sup>6</sup> Instituto de Física de Cantabria, Avda. de los Castros s/n 39005, Santander, Spain.

<sup>7</sup> Dept. Física Moderna, Universidad de Cantabria, Avda. de los Castros s/n 39005, Santander, Spain.

<sup>8</sup> Astrophysikalisches Institut Potsdam, An der Sternwarte 16, Potsdam, Germany.

## ABSTRACT

We present the optical and UV emission line properties of 160 X-ray selected AGN taken from the RIXOS survey (including H $\alpha$ , H $\beta$ , [OIII] $\lambda$ 5007, MgII $\lambda$ 2798 and CIII] $\lambda$ 1909). This sample is believed to contain a mixture of absorbed and unabsorbed objects, with column densities up to  $\sim 4 \times 10^{21}$  cm $^{-2}$ . Although the distribution of the [OIII] $\lambda$ 5007 EW for the RIXOS AGN is typical of optically-selected samples, the Balmer line EWs are relatively low. This is consistent with the presence of a dust absorber between the broad and narrow line regions (e.g. a molecular torus), and intrinsically weak optical line emission. We find Baldwin effects in CIII] $\lambda$ 1909 and MgII $\lambda$ 2798, and a positive response of the MgII line to its ionizing continuum.

There is a strong correlation between the EW and FWHM of MgII, which may be similar to that seen in other samples for H $\beta$ . We demonstrate that this is consistent with models which suggest two line-emitting zones, a ‘very broad line region’ (VBLR) and an ‘intermediate line region’ (ILR). The correlation between EW and FWHM in MgII may be a physical characteristic of the ILR: e.g. the radiative acceleration of the line-emitting clouds; or it may reflect a geometric dependence, e.g. anisotropies in the line or continuum emission, or a smaller covering factor of the ILR at large distances.

We found no correlation between the H $\beta$  FWHM and the slope of the X-ray spectrum, despite reports of correlations in other samples. However, this may be due to the effects of dust absorption which suppresses the broad H $\beta$  component, masking any relationship. The H $\alpha$  FWHM does tend to be narrow when  $\alpha_x$  is soft, and broadens as  $\alpha_x$  hardens, although the formal probability for this correlation is low (91 per cent). If the distribution of  $\alpha_x$  in the RIXOS sample reflects the level of intrinsic absorption in these AGN, the data suggest a possible link between the velocity of the Balmer line-emitting region and the amount of absorbing material beyond

**Key words:** Quasars: general – galaxies: active – galaxies: Seyfert – X-rays: general – line: formation – quasars: emission lines.

## 1 INTRODUCTION

The investigation and interpretation of the broad emission line properties of Seyferts and quasars is a complex task. Photoionization codes such as CLOUDY (Ferland 1993) and ION (Netzer 1993) have been successful at reproducing the observed ratios of many emission lines (e.g. Ferland & Netzer 1979; Kwan & Krolik 1981; Rees, Netzer & Ferland 1989), which supports photoionization as the most likely physical means of line production in AGN. However, finding an appropriate structure and geometry for the broad line region (BLR) has been less straightforward.

Many different models have been proposed for the BLR

structure, often invoking separate regions for the high- and low-ionization lines (HILs and LILs respectively). For example, models based on the intensive NGC 5548 monitoring campaign (Clavel et al. 1991; Peterson et al. 1991) suggest that the HILs (e.g. Ly $\alpha$ , CIII], CIV, HeI, HeII) are emitted from an inner, roughly spherical high-ionization zone while the LILs (which include most of the Balmer lines and MgII) are emitted from an outer, flattened low-ionization zone (Krolik et al. 1991; O’Brien, Goad & Gondhalekar 1994). Alternatively, it has been proposed that the HILs are emitted from an outflow aligned with the radio axis, while the LILs come from a flattened region lying in a plane perpendicular to the outflow (e.g. Wills et al. 1993). In the Collin-Souffrin

et al. (1988) model, the LILs are formed in the outer parts of an accretion disc while the HILs are produced in clouds of cooling gas behind shocks in a hypersonic flow of interstellar matter. The winds or envelopes of bloated stars have also been discussed as an origin of the BLR (e.g. Edwards 1980, Alexander & Netzer 1994; Baldwin et al. 1996).

The viability of these models can be tested using the observed emission line parameters of AGN, e.g. the full width at half maximum (FWHM) of the line, its luminosity and equivalent width (EW). The proximity of the BLR to the ionizing continuum source suggests that much of the line emission is directed from the inner face of a BLR cloud towards the central source (Ferland et al. 1992); for certain geometries (e.g. disc-shaped regions) this introduces a degree of anisotropy into the model which may be reflected in the fluxes and EWs of the lines. The FWHM, assuming that they are dominated by velocity broadening, measure the line-of-sight component of the velocity of the line-emitting gas. If the BLR is flattened so that the dominant motion of the clouds lies in a plane, the observed FWHM will also be a function of the viewing angle (i.e. the angle between our line of sight and the axis of the BLR).

We have used a sample of 160 X-ray selected AGN taken from the RIXOS survey (Mason et al. , in preparation) to test models of the BLR geometry in Seyfert 1s and quasars. The optical/UV and X-ray continuum properties of the RIXOS AGN are presented in Puchnarewicz et al. (1996a; hereafter Paper I). In this paper we present the emission line parameters of  $\text{CIII}\lambda 1909$ ,  $\text{MgII}\lambda 2798$ ,  $\text{H}\alpha$ ,  $\text{H}\beta$  and  $[\text{OIII}]\lambda 5007$  (see Section 2) and discuss sample properties and correlations for emission lines and continua (Sections 3 and 4). No redshift restriction has been placed on the sample, therefore the lines measured for each AGN depend on that AGN's redshift. This effectively results in five smaller 'subsamples', one for each emission line, which are compared with other line and continuum parameters. The implications of the results for the structure of the BLR and the geometry of the central regions in AGN, taking into account the effects of absorption (which are expected to be significant; see Paper I), are discussed in Section 5.

## 2 DATA REDUCTION

### 2.1 The RIXOS Survey

The RIXOS survey is compiled from serendipitous sources detected in pointed observations made with the *ROSAT* Position Sensitive Proportional Counter (PSPC; Pfeffermann et al. 1986). To be included in the survey, an observation must have an exposure time of at least 8 ksec and it must have been taken at a Galactic latitude greater than  $28^\circ$ . Only sources within 17 arcmin of the centre of the field and with a flux greater than  $3 \times 10^{-14}$  erg cm $^{-2}$  sec $^{-1}$  in the *ROSAT* 'hard' band (0.4-2.0 keV) are used; optical identification of survey sources is 94 per cent complete to this flux level over 15 deg $^2$ .

In total, 160 broad-line AGN (i.e. including Seyfert 1s to 1.9s and quasars) from the RIXOS survey are included in this analysis, covering a range in redshift from 0.03 to 2.92. Objects were included in this sample if they exhibited an unambiguous detection of redshifted line emission, and if the permitted line width was resolved and broad (i.e. with

a FWHM  $\gtrsim 1000$  km s $^{-1}$ ). At redshifts of around 1.0, the only strong line which falls within the observed range is MgII, thus if only a single broad emission line was observed and the expected positions of H $\beta$  and CIII] were not covered by the spectrum, the line was assumed to be MgII. At  $z \sim 0.3$ -0.4 the only permitted line observed is H $\beta$ . If the H $\beta$  line is narrow then this object will have been classified as a narrow emission line galaxy (NELG). However, it is also possible that these objects may be Seyfert 1.9s or similar where the broad component of H $\beta$  is suppressed or obscured. There are four RIXOS objects, classified as NELGs, which may be Seyfert 1.9s; F226\_74, F254\_6, F272\_10 and F273\_23; these are not included here but will be presented with other RIXOS NELGs in Romero-Colmenero et al. (in preparation). Four AGN from the complete sample whose X-ray spectra were poorly determined have been excluded from this paper; emission line data for a further six were not available, either because their redshift was too high to measure even CIII], or because they were catalogue identifications for which the relevant data could not be found from other references. The full RIXOS source list including X-ray and optical positions, fluxes etc., will be presented in a future paper (Mason et al. , in preparation).

**Table 1.** Optical and UV emission line parameters.

FID	SNo	z	H $\alpha$ $\lambda$ 6562			H $\beta$ $\lambda$ 4861			[OIII] $\lambda$ 5007			MgII $\lambda$ 2798			CIII] $\lambda$ 1909		
			lum	ew	fw hm	lum	ew	fw hm	lum	ew	fw hm	lum	ew	fw hm	lum	ew	fw hm
110	1	0.365	—	—	—	42.1 <sup>b</sup>	50 <sup>b</sup>	2900 <sup>b</sup>	41.9	30	700	41.9	20	1900	—	—	—
						42.0 <sup>n</sup>	20 <sup>n</sup>	900 <sup>n</sup>									
110	8	0.938	—	—	—	—	—	—	—	—	—	42.9	80	8000	—	—	—
110	35	0.582	—	—	—	42.0 <sup>u</sup>	50 <sup>u</sup>	1500 <sup>u</sup>	42.2	90	400	42.1 <sup>b</sup>	30 <sup>b</sup>	1900 <sup>b</sup>	—	—	—
												42.4 <sup>v</sup>	70 <sup>v</sup>	8500 <sup>v</sup>			
110	50	1.335	—	—	—	—	—	—	—	—	—	42.8	20	4100	43.0	20	4700
122	1	1.134	—	—	—	—	—	—	—	—	—	43.0 <sup>b</sup>	10 <sup>b</sup>	1100 <sup>b</sup>	43.2	10	7100
												43.8 <sup>v</sup>	40 <sup>v</sup>	9200 <sup>v</sup>			
122	13	0.358	—	—	—	41.4	10	3600 <sup>u</sup>	42.0	50	800	—	—	—	—	—	—
122	14	0.380	—	—	—	42.3 <sup>b</sup>	60 <sup>b</sup>	3100 <sup>b</sup>	41.8	20	500	42.3	20	2500	—	—	—
						41.8 <sup>n</sup>	10 <sup>n</sup>	1200 <sup>n</sup>									
122	21	0.376	—	—	—	42.1	30	1600 <sup>u</sup>	42.2	50	600	42.0 <sup>l</sup>	60 <sup>l</sup>	2000 <sup>f</sup>	—	—	—
123	1	0.281	—	—	—	42.3	70	3000	41.9	30	400	—	—	—	—	—	—
123	27	0.351	—	—	—	41.5 <sup>b</sup>	30 <sup>b</sup>	2400 <sup>b,u</sup>	41.6	40	400	—	—	—	—	—	—
						40.8 <sup>n</sup>	10 <sup>n</sup>	400 <sup>n</sup>									
123	28	0.212	41.8	40	2200	41.1	10	5100 <sup>u</sup>	41.1	10	500	—	—	—	—	—	—
123	41	1.821	—	—	—	—	—	—	—	—	—	43.4	10	2600	43.8	20	5200
123	42	0.476	—	—	—	41.3 <sup>b</sup>	20 <sup>b</sup>	2200 <sup>b,u</sup>	41.4	20	400	41.8	30	3000	—	—	—
						40.7 <sup>n</sup>	10 <sup>n</sup>	300 <sup>n</sup>									
123	46	1.288	—	—	—	—	—	—	—	—	—	43.4	40	5700	41.9 <sup>l</sup>	70 <sup>l</sup>	6000 <sup>f</sup>
123	66	0.494	—	—	—	42.2	50	3800 <sup>u</sup>	42.4	80	500	42.3	40	8000	—	—	—
123	85	0.652	—	—	—	42.3	20	1100 <sup>u</sup>	41.7	10	300	42.4	10	1700	—	—	—
125	14	1.833	—	—	—	—	—	—	—	—	—	43.8	30	4200	43.6	20	6400
125	17	0.449	—	—	—	42.1 <sup>b</sup>	60 <sup>b</sup>	2500 <sup>b</sup>	41.8	30	400	42.1	20	2500	—	—	—
						41.3 <sup>n</sup>	10 <sup>n</sup>	400 <sup>n</sup>									
126	1	0.028	41.0 <sup>b</sup>	60 <sup>b</sup>	4800 <sup>b</sup>	40.3	10	4800 <sup>u</sup>	40.3	10	400	—	—	—	—	—	—
			40.4 <sup>n</sup>	10 <sup>n</sup>	800 <sup>n</sup>												
133	22	1.788	—	—	—	—	—	—	—	—	—	44.3	20	4300	44.5	20	5800
205	1	0.717	—	—	—	—	—	—	—	—	—	42.5	30	2400	—	—	—
205	1	1.334	—	—	—	—	—	—	—	—	—	43.0	20	3500	—	—	—
205	22	0.445	—	—	—	42.6	80	5400	41.6	10	800	42.4	20	4000	—	—	—
205	23	0.618	—	—	—	41.9 <sup>u</sup>	30 <sup>u</sup>	1100 <sup>u</sup>	42.0	30	700	41.9 <sup>l</sup>	40 <sup>l</sup>	2000 <sup>f</sup>	—	—	—
205	34	0.755	—	—	—	—	—	—	—	—	—	42.3	50	5700	—	—	—
206	6	0.692	—	—	—	42.3	30	2400 <sup>u</sup>	—	—	—	42.7	40	3500	—	—	—
206	9	0.801	—	—	—	—	—	—	—	—	—	42.4	30	2700	—	—	—
206	507	0.484	—	—	—	41.1	10	2400 <sup>u</sup>	41.4	20	400	41.9	200	3800	—	—	—
206	522	0.740	—	—	—	—	—	—	—	—	—	42.3	10	2300	—	—	—
208	2	0.387	—	—	—	41.9	20	3900 <sup>u</sup>	41.8	20	600	42.2	30	2700	—	—	—
208	18	0.470	42.7	110	2100	42.0 <sup>b</sup>	20 <sup>b</sup>	3100 <sup>b</sup>	41.9	20	1500	42.6 <sup>b</sup>	30 <sup>b</sup>	2600 <sup>b</sup>	—	—	—
						41.7 <sup>n</sup>	10 <sup>n</sup>	1100 <sup>n</sup>				43.0 <sup>v</sup>	70 <sup>v</sup>	16700 <sup>v</sup>			
208	55	1.718	—	—	—	—	—	—	—	—	—	44.0	60	9800	43.7	30	7700
211	30	1.419	—	—	—	—	—	—	—	—	—	43.3	10	2000	44.0	20	8400
211	35	0.465	—	—	—	42.0 <sup>l</sup>	60 <sup>l</sup>	6000 <sup>f</sup>	41.2	10	500	42.4	90	5600	—	—	—
211	42	0.232	42.6 <sup>b</sup>	110 <sup>b</sup>	2200 <sup>b</sup>	42.0	30	2400	41.9	20	1300	—	—	—	—	—	—
			41.6 <sup>n</sup>	10 <sup>n</sup>	400 <sup>n</sup>												
212	6	1.000	—	—	—	—	—	—	—	—	—	43.2	30	3700	—	—	—
212	16	0.842	—	—	—	—	—	—	—	—	—	42.8	50	9100	—	—	—
212	25	0.802	—	—	—	—	—	—	—	—	—	42.9	40	6700	—	—	—
212	32	0.927	—	—	—	—	—	—	—	—	—	43.1	20	6200	—	—	—
212	32	0.924	—	—	—	—	—	—	—	—	—	43.3	30	5100	—	—	—
213	7	0.542	—	—	—	41.4	10	3900 <sup>u</sup>	41.9	40	600	42.3	50	3300	—	—	—
213	11	1.546	—	—	—	—	—	—	—	—	—	43.2	60	7400	43.2	30	9600
213	17	0.438	—	—	—	41.8 <sup>b</sup>	30 <sup>b</sup>	4500 <sup>b</sup>	41.7	30	900	42.5	60	4100	—	—	—
						40.7 <sup>n</sup>	10 <sup>n</sup>	300 <sup>n</sup>									
213	19	0.467	—	—	—	42.1	40	3000	41.4	10	600	42.0	20	2000	—	—	—
213	20	0.664	—	—	—	43.1	60	4700	42.3	10	400	42.9	20	2500	—	—	—
215	1	2.249	—	—	—	—	—	—	—	—	—	44.2	10	2900	44.4	10	5000
215	19	0.584	—	—	—	42.7	40	2300 <sup>u</sup>	43.2	110	100	42.4	10	1600	—	—	—

**Table 1** (continued): Optical and UV emission line parameters.

FID	SNo	z	H $\alpha$ $\lambda$ 6562			H $\beta$ $\lambda$ 4861			[OIII] $\lambda$ 5007			MgII $\lambda$ 2798			CIII] $\lambda$ 1909		
			lum	ew	fw hm	lum	ew	fw hm	lum	ew	fw hm	lum	ew	fw hm	lum	ew	fw hm
215	32	0.612	—	—	—	42.8 <sup>u</sup>	90 <sup>u</sup>	3700 <sup>u</sup>	41.6	10	600	42.5	20	2700	—	—	—
216	7	0.804	—	—	—	—	—	—	—	—	—	43.2	50	5500	—	—	—
216	30	0.941	—	—	—	—	—	—	—	—	—	43.0 <sup>u</sup>	210 <sup>u</sup>	7400 <sup>u</sup>	—	—	—
216	33	0.792	—	—	—	42.8 <sup>l</sup>	90 <sup>l</sup>	5000 <sup>f</sup>	42.4 <sup>l</sup>	30 <sup>l</sup>	1000 <sup>f</sup>	42.5 <sup>b</sup>	10 <sup>b</sup>	3200 <sup>b</sup>	—	—	—
									42.6 <sup>v</sup>	20 <sup>v</sup>	6500 <sup>v</sup>	—	—	—			
217	3	0.989	—	—	—	—	—	—	—	—	—	43.3	40	4600	—	—	—
217	21	0.561	—	—	—	42.2 <sup>l</sup>	20 <sup>l</sup>	5000 <sup>f</sup>	41.4	10	700	42.0	30	4900	—	—	—
217	34	1.199	—	—	—	—	—	—	—	—	—	43.2	20	3900	43.7 <sup>u</sup>	420 <sup>u</sup>	5500 <sup>u</sup>
217	35	0.435	—	—	—	41.4	10	3300	41.9	30	500	42.4	60	4600	—	—	—
217	59	0.587	—	—	—	42.3 <sup>l</sup>	100 <sup>l</sup>	9000 <sup>f</sup>	41.5 <sup>l</sup>	20 <sup>l</sup>	1000 <sup>f</sup>	42.4	90	9300	—	—	—
218	1	0.545	—	—	—	43.0 <sup>b</sup>	60 <sup>b</sup>	7400 <sup>b</sup>	42.6	30	500	43.2	40	5000	—	—	—
						41.6 <sup>n</sup>	10 <sup>n</sup>	400 <sup>n</sup>									
218	9	0.703	—	—	—	—	—	—	—	—	—	42.6	30	4100	—	—	—
218	14	0.224	41.7 <sup>b</sup>	100 <sup>b</sup>	2700 <sup>b</sup>	40.8	10	1700	41.2	30	400	—	—	—	—	—	—
						41.0 <sup>n</sup>	20 <sup>n</sup>	600 <sup>n</sup>									
218	21	0.79 <sup>u</sup>	—	—	—	—	—	—	—	—	—	41.9 <sup>u</sup>	20 <sup>u</sup>	4700 <sup>u</sup>	—	—	—
218	27	0.629	—	—	—	43.0	50	2400	42.4	10	900	43.1	30	3300	—	—	—
219	15	1.186	—	—	—	—	—	—	—	—	—	43.0	20	2600	43.1	30	4900
219	45	1.272	—	—	—	—	—	—	—	—	—	43.4	70	6600	41.9 <sup>l</sup>	770 <sup>l</sup>	6000 <sup>f</sup>
219	48	1.373	—	—	—	—	—	—	—	—	—	43.0	30	9000	43.0	20	6600
220	13	0.968	—	—	—	—	—	—	—	—	—	42.6	10	3600	—	—	—
220	18	0.442	—	—	—	41.4 <sup>u</sup>	20 <sup>u</sup>	1800 <sup>u</sup>	41.9	50	600	42.4	90	10100	—	—	—
220	23	0.193	42.5 <sup>u</sup>	70 <sup>u</sup>	2000 <sup>u</sup>	41.5 <sup>u</sup>	10 <sup>u</sup>	1200 <sup>u</sup>	41.5	10	500	—	—	—	—	—	—
221	2	0.900	—	—	—	42.5 <sup>u</sup>	20 <sup>u</sup>	1900 <sup>u</sup>	42.8	40	400	42.9	20	2300	—	—	—
221	7	0.292	—	—	—	42.2	30	2300	42.1	20	800	—	—	—	—	—	—
221	16	0.184	41.8	80	1300	41.2	20	1700	41.0	10	400	—	—	—	—	—	—
221	35 <sup>r1</sup>	0.451	44.1	460	2800	43.5	130	4600	43.4	110	800	43.5	50	2400	—	—	—
223	17	0.288	—	—	—	42.1 <sup>b</sup>	30 <sup>b</sup>	4000 <sup>b</sup>	41.7	10	500	—	—	—	—	—	—
						41.6 <sup>n</sup>	10 <sup>n</sup>	900 <sup>n</sup>									
224	201	1.547	—	—	—	—	—	—	—	—	—	43.7	50	8100	43.7	30	7400
225	1	0.487	—	—	—	42.7	50	2900 <sup>u</sup>	42.5	70	1000	43.0 <sup>l</sup>	120 <sup>l</sup>	3000 <sup>f</sup>	—	—	—
226	41	1.316	—	—	—	—	—	—	—	—	—	43.1	10	6400	43.8	30	5200
226	114	1.021	—	—	—	—	—	—	—	—	—	42.5	70	2300	—	—	—
227	19	1.859	—	—	—	—	—	—	—	—	—	43.4	10	1700	43.9	20	6800
227	37	1.417	—	—	—	—	—	—	—	—	—	44.3	60	6700	44.2	50	9000
227	513	0.958	—	—	—	—	—	—	—	—	—	43.2	30	3600	—	—	—
228	1	1.722	—	—	—	—	—	—	—	—	—	44.4	40	11300	43.9	10	2400
232	16	0.227	42.0 <sup>b</sup>	100 <sup>b</sup>	2400 <sup>b</sup>	41.5	30	2100	41.2	10	400	—	—	—	—	—	—
						40.7 <sup>n</sup>	10 <sup>n</sup>	200 <sup>n</sup>									
232	301	0.384	42.9	120	2600	42.3	40	3300	42.3	40	900	—	—	—	—	—	—
234	1	1.651	—	—	—	—	—	—	—	—	—	44.2	30	6000	43.3	0	11800
234	33	1.026	—	—	—	—	—	—	—	—	—	43.0	20	7600	43.0	10	6300
236	5	0.473	42.6	60	1300	42.2	40	2400 <sup>u</sup>	41.7	10	500	42.4	30	3100	—	—	—
236	21	1.128	—	—	—	—	—	—	—	—	—	43.1	40	2800	43.5	130	8300
236	22	0.048	41.5	70	3400	40.8	20	2700 <sup>u</sup>	40.5	10	600	—	—	—	—	—	—
238	11	0.325	—	—	—	42.1	80	6300 <sup>u</sup>	41.3	20	500	—	—	—	—	—	—
240	15	1.277	—	—	—	—	—	—	—	—	—	42.7	10	2100	42.8	10	6300
240	82	0.519	—	—	—	42.1	30	7400	—	—	—	42.6	30	8600	—	—	—
245	4	0.711	—	—	—	—	—	—	—	—	—	42.7	100	9300	—	—	—
248	2	0.274	42.0	180	2300	41.6 <sup>l</sup>	160 <sup>l</sup>	2000 <sup>f</sup>	41.3	60	800	—	—	—	—	—	—
248	51 <sup>r2</sup>	0.242	42.7	170	3000	42.4	80	3200	41.8	20	500	—	—	—	—	—	—
252	1	0.219	—	—	—	42.3 <sup>l</sup>	90 <sup>l</sup>	2000 <sup>f</sup>	42.0	30	700	—	—	—	—	—	—
252	9	0.673	—	—	—	42.1	30	1900 <sup>u</sup>	—	—	—	42.8	40	5800	—	—	—
252	31*	1.413	—	—	—	—	—	—	—	—	—	44.1 <sup>u</sup>	10 <sup>u</sup>	2800 <sup>u</sup>	44.1	10	5900
252	31*	1.415	—	—	—	—	—	—	—	—	—	44.1 <sup>u</sup>	10 <sup>u</sup>	2800 <sup>u</sup>	44.1	10	5900
252	34	0.679	—	—	—	—	—	—	—	—	—	42.3	50	5500	—	—	—
252	36	1.038	—	—	—	—	—	—	—	—	—	43.2	90	6000	42.9	40	4500
252	38	0.216	42.3 <sup>b</sup>	230 <sup>b</sup>	1600 <sup>b</sup>	41.6 <sup>b</sup>	40 <sup>b</sup>	1300 <sup>b,u</sup>	41.9	80	400	—	—	—	—	—	—
						41.7 <sup>n</sup>	50 <sup>n</sup>	300 <sup>n</sup>	40.9 <sup>n</sup>	10 <sup>n</sup>	300 <sup>n</sup>	41.9	80	400	—	—	—
252	46 <sup>r3</sup>	2.091	—	—	—	—	—	—	—	—	—	—	60	15300	—	80	6300

**Table 1** (continued): Optical and UV emission line parameters.

FID	SNo	z	H $\alpha$ λ6562			H $\beta$ λ4861			[OIII]λ5007			MgIIλ2798			CIII]λ1909		
			lum	ew	fw hm	lum	ew	fw hm	lum	ew	fw hm	lum	ew	fw hm	lum	ew	fw hm
253	5	1.204	—	—	—	—	—	—	—	—	—	43.1	40	6300	43.2	30	11600
254	10	0.935	—	—	—	44.3	40	2600	44.2	30	1100	44.0	10	2700	44.2	10	3400
254	11	1.166	—	—	—	—	—	—	—	—	—	44.1	20	4100	44.2	20	9700
254	41	0.486	—	—	—	42.4	50	6900	41.6	10	700	42.7	40	8000	—	—	—
255	7	0.260	41.8	70	2100	41.0 <sup>l</sup>	20 <sup>l</sup>	4000 <sup>f</sup>	40.9	10	500	—	—	—	—	—	—
255	13	0.581	—	—	—	42.4 <sup>l</sup>	120 <sup>l</sup>	4000 <sup>f</sup>	42.0 <sup>l</sup>	50 <sup>l</sup>	1000 <sup>f</sup>	42.5	40	3900	—	—	—
255	19	0.862	—	—	—	—	—	—	—	—	—	42.9	30	5000	—	—	—
255	23	0.759	—	—	—	—	—	—	—	—	—	42.8 <sup>u</sup>	80 <sup>u</sup>	14100 <sup>u</sup>	—	—	—
257	1	1.029	—	—	—	—	—	—	—	—	—	43.7 <sup>u</sup>	10 <sup>u</sup>	14100 <sup>u</sup>	43.6 <sup>u</sup>	10 <sup>u</sup>	8800 <sup>u</sup>
257	14	1.096	—	—	—	—	—	—	—	—	—	42.3	40	2300	42.6 <sup>u</sup>	850 <sup>u</sup>	3400 <sup>u</sup>
257	20	1.302	—	—	—	—	—	—	—	—	—	43.5	20	5700	43.6 <sup>u</sup>	20 <sup>u</sup>	10900 <sup>u</sup>
257	37	0.329	—	—	—	40.7 <sup>u</sup>	20 <sup>u</sup>	300 <sup>u</sup>	40.9	40	400	—	—	—	—	—	—
257	38	1.260	—	—	—	—	—	—	—	—	—	43.8	20	4400	43.9	10	10300
258	1	0.698	—	—	—	41.9	10	600 <sup>u</sup>	—	—	—	42.3 <sup>u</sup>	40 <sup>u</sup>	3300 <sup>u</sup>	—	—	—
258	5	0.811	—	—	—	—	—	—	—	—	—	42.6	20	2200	—	—	—
258	30	0.847	—	—	—	—	—	—	—	—	—	42.5	30	5000	—	—	—
258	32	1.615	—	—	—	—	—	—	—	—	—	43.3 <sup>u</sup>	20 <sup>u</sup>	5500 <sup>u</sup>	42.7 <sup>b</sup>	10 <sup>b</sup>	1200 <sup>b</sup>
															43.2 <sup>v</sup>	10 <sup>v</sup>	10200 <sup>v</sup>
259	5	0.984	—	—	—	—	—	—	—	—	—	43.1	40	8400	42.8	10	5300
259	7	0.408	—	—	—	41.9	40	1900	41.5	20	600	41.9	20	3200	—	—	—
259	11	0.995	—	—	—	—	—	—	—	—	—	42.9	50	5800	42.2 <sup>u</sup>	10 <sup>u</sup>	5500 <sup>u</sup>
260	8	1.822	—	—	—	—	—	—	—	—	—	44.3	10	7400	44.5	20	4600
260	44	1.502	—	—	—	—	—	—	—	—	—	43.6	30	3500	43.6	20	4100
262	1	0.882	—	—	—	—	—	—	—	—	—	43.0	50	4800	—	—	—
262	12	0.923	—	—	—	43.5 <sup>l</sup>	540 <sup>l</sup>	5000 <sup>f</sup>	43.0 <sup>l</sup>	180 <sup>l</sup>	1000 <sup>f</sup>	43.0 <sup>b</sup>	20 <sup>b</sup>	3100 <sup>b</sup>	43.0	30	2100
												42.9 <sup>v</sup>	20 <sup>v</sup>	8700 <sup>v</sup>			
262	34	0.311	42.6 <sup>b</sup>	250 <sup>b</sup>	6300 <sup>b</sup>	42.3	60	4300	41.6	10	700	42.4	40	3900	—	—	—
			42.6 <sup>n</sup>	120 <sup>n</sup>	1660 <sup>n</sup>												
265	1	2.336	—	—	—	—	—	—	—	—	—	—	—	—	42.2 <sup>l</sup>	10 <sup>l</sup>	9000 <sup>f</sup>
265	17	0.448	—	—	—	41.9	40	3400	41.3	10	400	41.8	10	1900	—	—	—
268	11	1.189	—	—	—	—	—	—	—	—	—	42.7	50	7900	42.7	60	7600
268	24	0.252	42.5 <sup>b</sup>	80 <sup>b</sup>	2100 <sup>b</sup>	42.2	30	3800 <sup>u</sup>	41.5	10	800	—	—	—	—	—	—
			42.1 <sup>n</sup>	30 <sup>n</sup>	800 <sup>n</sup>												
271	2	0.444	43.0	240	2900	41.9	10	1400 <sup>u</sup>	41.5	10	800	42.4	40	3100	—	—	—
271	7	1.035	—	—	—	—	—	—	—	—	—	43.2	20	4300	43.3	20	7000
272	8	1.817	—	—	—	—	—	—	—	—	—	43.3	30	3500	43.1	10	4600
272	18	0.604	—	—	—	42.5 <sup>b</sup>	30 <sup>b</sup>	4400 <sup>b</sup>	42.4	20	600	43.1	50	6100	—	—	—
			41.6 <sup>n</sup>	10 <sup>n</sup>	400 <sup>n</sup>												
272	23	0.096	41.9	130	2600	41.3	50	5900 <sup>u</sup>	41.3	50	1400	—	—	—	—	—	—
272	28	0.444	—	—	—	40.9 <sup>u</sup>	10 <sup>u</sup>	600 <sup>u</sup>	42.0	30	600	42.4	100	6500	—	—	—
273	4	1.045	—	—	—	—	—	—	—	—	—	43.6	20	2600	43.6	10	4100
273	6	0.269	43.2	230	9200	42.5	40	11000	41.6	10	1000	—	—	—	—	—	—
273	18	0.361	—	—	—	41.7	40	2600	41.9	70	500	41.7	20	4500	—	—	—
273	22	1.075	—	—	—	—	—	—	—	—	—	43.9	10	3700	43.9	10	7700
274	8	0.156	42.3	50	1200	41.9	20	2200	41.9	20	900	—	—	—	—	—	—
278	9	0.948	—	—	—	43.7	50	2600	42.9	10	800	43.6	20	3800	43.7	10	5600
278	10	0.091	42.9 <sup>b</sup>	260 <sup>b</sup>	7100 <sup>b</sup>	41.6	10	800 <sup>u</sup>	42.6	120	800	—	—	—	—	—	—
			42.5 <sup>n</sup>	60 <sup>n</sup>	1300 <sup>n</sup>												
281	11	2.919	—	—	—	—	—	—	—	—	—	—	—	—	43.5	10	4300
281	21	0.347	42.7	170	3200	42.4	90	9100 <sup>u</sup>	41.6	20	700	42.3	200	5300	—	—	—
283	6	1.219	—	—	—	—	—	—	—	—	—	44.1	30	5200	43.9	20	4200
283	11	0.272	43.1 <sup>b</sup>	180 <sup>b</sup>	3500 <sup>b</sup>	42.5 <sup>b</sup>	30 <sup>b</sup>	4900 <sup>b</sup>	42.0	10	1200	—	—	—	—	—	—
			42.6 <sup>n</sup>	60 <sup>n</sup>	1700 <sup>n</sup>	42.0 <sup>n</sup>	10 <sup>n</sup>	1600 <sup>n</sup>									
283	14	0.284	42.5 <sup>b</sup>	110 <sup>b</sup>	3900 <sup>b</sup>	42.3	40	3300	41.8	20	1600	—	—	—	—	—	—
			42.4 <sup>n</sup>	70 <sup>n</sup>	1700 <sup>n</sup>												
283	21	0.719	—	—	—	43.3 <sup>l</sup>	170 <sup>l</sup>	6000 <sup>f</sup>	42.7	50	1400	43.0	40	6300	—	—	—
286	2	1.498	—	—	—	—	—	—	—	—	—	44.4	30	9800	44.0	10	11900
290	21	2.573	—	—	—	—	—	—	—	—	—	—	—	—	44.5	10	4800

**Table 1** (continued): Optical and UV emission line parameters.

FID	SNo	z	H $\alpha$ $\lambda$ 6562			H $\beta$ $\lambda$ 4861			[OIII] $\lambda$ 5007			MgII $\lambda$ 2798			CIII] $\lambda$ 1909		
			lum	ew	fw $hm$	lum	ew	fw $hm$	lum	ew	fw $hm$	lum	ew	fw $hm$	lum	ew	fw $hm$
293	1	0.824	—	—	—	—	—	—	—	—	—	43.1	50	3200	—	—	—
293	6	0.081	42.2	70	1900	41.8 <sup>l</sup>	20 <sup>l</sup>	2000 <sup>f</sup>	41.4	10	1000	—	—	—	—	—	—
293	10	0.758	—	—	—	—	—	—	—	—	—	42.7 <sup>b</sup>	20 <sup>b</sup>	3000 <sup>b</sup>	—	—	—
												43.1 <sup>v</sup>	50 <sup>v</sup>	14200 <sup>v</sup>			
293	12	0.917	—	—	—	42.6 <sup>u</sup>	20 <sup>u</sup>	1800 <sup>u</sup>	42.8 <sup>l</sup>	60 <sup>l</sup>	1000 <sup>f</sup>	42.7	20	2500	42.8	10	3900
293	13	0.189	41.2 <sup>u</sup>	80 <sup>u</sup>	1700 <sup>u</sup>	41.1 <sup>l</sup>	70 <sup>l</sup>	2000 <sup>f</sup>	40.3	10	200	—	—	—	—	—	—
294	1	0.713	—	—	—	—	—	—	—	—	—	42.8	50	8200	—	—	—
302	14	0.809	—	—	—	43.1 <sup>l</sup>	120 <sup>l</sup>	2000 <sup>f</sup>	42.8 <sup>l</sup>	60 <sup>l</sup>	1000 <sup>f</sup>	42.9	20	2200	—	—	—
302	18	0.924	—	—	—	—	—	—	—	—	—	43.7	40	3300	—	—	—
305	11	0.251	42.0	90	3500	41.7	30	5500 <sup>u</sup>	41.3	10	700	42.4 <sup>u</sup>	170 <sup>u</sup>	5900 <sup>u</sup>	—	—	—
305	18	0.387	42.3 <sup>b</sup>	110 <sup>b</sup>	3800 <sup>b</sup>	41.9	30	2900 <sup>u</sup>	41.7	20	600	42.1	30	3100	—	—	—
			41.8 <sup>n</sup>	30 <sup>n</sup>	500 <sup>n</sup>												
305	34	0.854	—	—	—	42.4 <sup>u</sup>	30 <sup>u</sup>	1400 <sup>u</sup>	42.4	50	500	42.6	30	2100	—	—	—
Sample statistics																	
		z	H $\alpha$ $\lambda$ 6562			H $\beta$ $\lambda$ 4861			[OIII] $\lambda$ 5007			MgII $\lambda$ 2798			CIII] $\lambda$ 1909		
			lum	ew	fw $hm$	lum	ew	fw $hm$	lum	ew	fw $hm$	lum	ew	fw $hm$	lum	ew	fw $hm$
median		0.719	42.3	110	2600	42.1	34	3300	41.8	20	—	42.9	29	3900	43.6	16	5800
mean		0.82	42.9	140	3100	42.8	38	3900	42.5	29	—	43.4	37	4600	43.9	22	6300
$\sigma$		0.53	0.6	90	1800	0.7	23	2000	0.8	26	—	0.5	30	2300	0.4	21	2600
error		0.04	0.2	20	400	0.2	3	400	0.2	3	—	0.1	3	200	0.1	3	400

FID: RIXOS field number, SNo: RIXOS source number, z: AGN redshift, lum: Logarithm of the line luminosity in ergs s $^{-1}$ , ew: Rest-frame equivalent width in Å, fwhm: FWHM in km s $^{-1}$ ; <sup>b</sup> broad component only; <sup>n</sup> narrow component only; <sup>v</sup> very broad component only; <sup>u</sup> parameter uncertain; <sup>l</sup> line luminosities and EWs are upper limits; <sup>f</sup> FWHM fixed (i.e. for calculating upper limits); <sup>r1</sup> data from Puchnarewicz et al. (1992); <sup>r2</sup> data from Stephens (1989); <sup>r3</sup> data from Brotherton et al. (1994); \* F252\_31 is the double quasar E0957+561; the optical spectrum of only one component (from Puchnarewicz et al. 1992) was available and this was assumed to be the same for the other component as well. The median, mean,  $\sigma$  (i.e. standard deviation on the mean) and error on the mean have been calculated from the sample shown, excluding uncertain parameters and neglecting upper limits; source 6 in field 273 was also excluded because of its unusual nature (see Section 4.5.1). Where two components have been fitted to permitted line profiles, only the broad components are used for these statistics.

## 2.2 Optical

The optical spectra were obtained over several observing runs with the Isaac Newton (INT) and William Herschel Telescopes (WHT) at the Observatorio del Roque de los Muchachos, La Palma. Three different instruments were used, the Faint Object Spectrograph (FOS) and the Intermediate Dispersion Spectrograph (IDS) on the INT and the Intermediate-Dispersion Spectrograph and Imaging System (ISIS) on the WHT. The FOS spectra cover a range of 3500Å to 10000Å with a resolution of 15-20Å FWHM in the red and 8-10Å FWHM in the blue, while the IDS spectra cover the same range with a resolution of  $\sim$ 10Å FWHM. The ISIS spectra cover 3000Å to 9000Å with a resolution of 3Å FWHM in the red and 2Å in the blue. All spectra were taken using a narrow slit (typically  $\sim$ 1'' – 1.5'') which was positioned at the parallactic angle except where indicated in Table 2. On average, the seeing was  $\sim$ 1'' – 1.5''.

Photometrically-calibrated CCD images of 36 sources were also obtained at the INT, Jacobus Kapteyn (JKT), and Nordic Optical (NOT) Telescopes and these were used to check for the amount of light typically lost around the narrow slit. For these AGN, the average ratio of flux measured from the CCD images to flux measured from the spectra was  $1.2 \pm 0.1$  (error on the mean). Objects where there was a strong galactic contribution to the CCD images were

not included in the calculation of this ratio. Flux measurements from spectra where CCD images are available were corrected for any difference between spectral and CCD flux levels. Where CCD images are not available, the flux measured from the spectrum was increased by the mean factor of 1.2.

### 2.2.1 Line parameters

Due to the redshift coverage of the sample and the limited observed wavelength range, not all of the five emission lines discussed here (i.e. H $\alpha$ , H $\beta$ , [OIII], MgII and CIII]) could be measured for all AGN. Effectively, this produces five subsamples, one for each line. There are 30 measurements of H $\alpha$ , 71 measurements of H $\beta$  (plus 13 upper limits), 75 measurements of [OIII] $\lambda$ 5007 (plus 6 upper limits), 127 measurements of MgII (plus 3 upper limits) and 49 measurements of CIII] (plus 4 upper limits).

Line fluxes, positions, rest-frame equivalent widths (EWs) and FWHM were measured from the spectrum by fitting one or more Gaussian profiles to each line. Where the emission line of interest was blended with other lines or blends (such as FeII), additional Gaussians were used to model the contaminants. Where the line of interest could not be well represented by a single Gaussian profile, additional components were used. The continuum was modelled as a

**Table 2:** Optical/UV and X-ray continuum parameters.

FID	S No	Ins	z	$N_{\text{HGal}}$	$L_{2500}$	$L_{0.2\text{keV}}$	$L_{2\text{keV}}$	$\alpha_{\text{opt}}$	$\alpha_{\text{x}}$	$\alpha_{\text{os}}$	$\alpha_{\text{ox}}$
(1)	(2)	(3)	(4)	(5)	(6)	(7)	(8)	(9)	(10)	(11)	(12)
122	13	ISIS	0.358	4.1	$28.2^i$	$26.1^{+0.5}_{-0.6}$	$26.1^{+0.2}_{-0.2}$	3.1	$0.00^{+0.28}_{-0.28}$	$1.3^{+0.6}_{-0.5}$	$0.8^{+0.2}_{-0.2}$
122	21 <sup>(43)</sup>	ISIS	0.376	4.1	$28.5^i$	$26.4^{+0.5}_{-0.6}$	$26.2^{+0.2}_{-0.2}$	2.3	$0.23^{+0.26}_{-0.28}$	$1.3^{+0.6}_{-0.5}$	$0.9^{+0.2}_{-0.2}$
123	28	ISIS	0.212	1.2	$28.6^i$	$26.2^{+0.4}_{-0.4}$	$25.0^{+0.2}_{-0.2}$	np	$1.16^{+0.13}_{-0.14}$	$1.5^{+0.4}_{-0.4}$	$1.3^{+0.2}_{-0.2}$
125	14	ISIS	1.833	5.0	30.2	$28.6^{+0.9}_{-1.7}$	$27.7^{+0.2}_{-0.3}$	1.6	$0.96^{+0.40}_{-0.51}$	$1.0^{+1.2}_{-0.8}$	$1.0^{+0.2}_{-0.2}$
125	17 <sup>(36)</sup>	ISIS	0.449	5.0	28.9	$27.7^{+0.4}_{-0.5}$	$26.3^{+0.1}_{-0.1}$	0.6	$1.48^{+0.16}_{-0.20}$	$0.7^{+0.5}_{-0.4}$	$1.0^{+0.2}_{-0.2}$
126	1	ISIS	0.028	2.0	27.5	$24.0^{+0.5}_{-0.7}$	$23.9^{+0.4}_{-0.1}$	2.3 <sup>p</sup>	$0.14^{+0.33}_{-0.35}$	$2.1^{+0.6}_{-0.5}$	$1.4^{+0.2}_{-0.3}$
205	1	ISIS	0.717	4.3	29.2	$28.8^{+0.7}_{-1.0}$	$26.4^{+0.2}_{-0.2}$	0.6	$1.43^{+0.34}_{-0.32}$	$0.2^{+0.8}_{-0.6}$	$1.0^{+0.2}_{-0.2}$
205	1	ISIS	1.334	4.3	29.6	$28.6^{+0.8}_{-1.1}$	$27.2^{+0.2}_{-0.2}$	1.2	$1.43^{+0.34}_{-0.32}$	$0.6^{+0.9}_{-0.7}$	$0.9^{+0.2}_{-0.2}$
205	22	ISIS	0.445	4.3	29.3	$27.8^{+0.4}_{-0.4}$	$26.2^{+0.2}_{-0.2}$	0.4	$1.65^{+0.16}_{-0.17}$	$0.9^{+0.5}_{-0.4}$	$1.2^{+0.2}_{-0.2}$
205	23	ISIS	0.618	4.3	28.3	$27.6^{+0.6}_{-0.8}$	$26.5^{+0.2}_{-0.2}$	np	$1.14^{+0.27}_{-0.29}$	$0.4^{+0.7}_{-0.6}$	$0.7^{+0.2}_{-0.2}$
205	34	ISIS	0.755	4.3	$28.7^i$	$27.5^{+1.1}_{-1.8}$	$26.3^{+0.3}_{-0.3}$	0.9	$1.20^{+0.51}_{-0.62}$	$0.7^{+1.3}_{-0.8}$	$0.9^{+0.2}_{-0.2}$
206	507	ISIS	0.484	3.7	27.7	$26.8^{+0.7}_{-1.0}$	$25.9^{+0.3}_{-0.3}$	3.9	$0.98^{+0.34}_{-0.40}$	$0.5^{+0.8}_{-0.6}$	$0.7^{+0.2}_{-0.2}$
206	522	ISIS	0.740	3.7	29.3	$27.7^{+0.6}_{-0.7}$	$26.4^{+0.2}_{-0.2}$	-0.0	$1.37^{+0.23}_{-0.27}$	$0.9^{+0.6}_{-0.6}$	$1.1^{+0.2}_{-0.2}$
208	18	IDS	0.470	0.7	$29.3^i$	$27.6^{+0.3}_{-0.3}$	$26.1^{+0.1}_{-0.2}$	0.6	$1.49^{+0.11}_{-0.09}$	$1.0^{+0.4}_{-0.4}$	$1.2^{+0.2}_{-0.2}$
211	35 <sup>(18)</sup>	ISIS	0.465	4.0	$28.7^i$	$27.0^{+0.7}_{-1.0}$	$25.9^{+0.3}_{-0.3}$	1.8	$1.12^{+0.33}_{-0.40}$	$1.0^{+0.8}_{-0.6}$	$1.1^{+0.2}_{-0.2}$
212	32*	ISIS	0.927	1.2	30.0	$28.1^{+0.5}_{-0.5}$	$26.7^{+0.2}_{-0.2}$	-0.3	$1.46^{+0.12}_{-0.15}$	$1.2^{+0.5}_{-0.5}$	$1.3^{+0.2}_{-0.2}$
212	32*	ISIS	0.924	1.2	30.0	$28.1^{+0.5}_{-0.5}$	$26.7^{+0.2}_{-0.2}$	0.4	$1.46^{+0.12}_{-0.15}$	$1.1^{+0.5}_{-0.5}$	$1.3^{+0.2}_{-0.2}$
213	7	ISIS	0.542	4.4	28.7	$27.0^{+0.9}_{-1.3}$	$26.3^{+0.3}_{-0.1}$	1.0	$0.71^{+0.48}_{-0.57}$	$1.1^{+1.0}_{-0.8}$	$0.9^{+0.2}_{-0.2}$
213	11	ISIS	1.546	4.4	29.4	$26.1^u$	$26.9^u$	-0.1	$-0.49^{+1.0}_{-1.6}$	$2.0^u$	$0.9^u$
213	20	ISIS	0.664	4.4	29.8	$27.6^{+0.8}_{-1.2}$	$26.6^{+0.3}_{-0.3}$	0.5	$1.02^{+0.37}_{-0.47}$	$1.4^{+1.0}_{-0.7}$	$1.2^{+0.2}_{-0.2}$
216	30 <sup>(50)</sup>	ISIS	0.941	3.5	$28.8^i$	$27.8^{+0.6}_{-0.8}$	$26.8^{+0.1}_{-0.2}$	np	$0.99^{+0.26}_{-0.30}$	$0.6^{+0.7}_{-0.6}$	$0.8^{+0.2}_{-0.2}$
216	33	IDS	0.792	3.5	29.3	$27.5^{+0.8}_{-1.1}$	$26.5^{+0.2}_{-0.2}$	0.4	$1.04^{+0.35}_{-0.39}$	$1.1^{+0.9}_{-0.7}$	$1.1^{+0.2}_{-0.2}$
218	9	ISIS	0.703	3.0	29.3	$27.7^{+0.9}_{-1.1}$	$26.2^{+0.3}_{-0.4}$	0.2	$1.51^{+0.36}_{-0.36}$	$0.9^{+0.9}_{-0.8}$	$1.2^{+0.3}_{-0.2}$
218	13 <sup>(25)</sup>	HB	1.450	3.0	30.7	$28.1^{+1.3}_{-2.4}$	$27.1^{+0.3}_{-0.5}$	—	$1.01^{+0.54}_{-0.67}$	$1.6^{+1.7}_{-1.0}$	$1.4^{+0.3}_{-0.2}$
218	14 <sup>(25)</sup>	ISIS	0.224	3.0	27.7	$26.7^{+0.6}_{-0.7}$	$25.5^{+0.3}_{-0.3}$	2.6	$1.21^{+0.53}_{-0.80}$	$0.6^{+0.6}_{-0.5}$	$0.9^{+0.2}_{-0.2}$
218	21	ISIS	0.790	3.0	28.7	$26.2^{+1.4}_{-2.7}$	$26.6^{+0.3}_{-0.4}$	np	$-0.32^{+0.68}_{-0.91}$	$1.6^{+1.9}_{-1.1}$	$0.8^{+0.3}_{-0.2}$
219	45 <sup>(28)</sup>	ISIS	1.272	1.3	$29.4^i$	$27.9^{+0.4}_{-0.4}$	$27.4^{+0.1}_{-0.1}$	2.4	$0.55^{+0.13}_{-0.14}$	$0.9^{+0.4}_{-0.4}$	$0.8^{+0.2}_{-0.2}$
220	13	ISIS	0.968	3.9	29.6	$25.0^u$	$26.5^u$	np	$-0.9^{+1.3}_{-1.8}$	$2.8^u$	$1.2^u$
220	18	ISIS	0.442	3.9	$28.8^i$	$26.7^{+1.1}_{-2.3}$	$25.9^{+0.6}_{-0.4}$	0.6	$0.78^{+0.57}_{-0.88}$	$1.3^{+1.6}_{-0.9}$	$1.1^{+0.3}_{-0.3}$
221	2	HB	0.900	2.9	29.6	$27.6^{+0.8}_{-1.2}$	$26.6^{+0.2}_{-0.2}$	0.4	$0.94^{+0.36}_{-0.39}$	$1.3^{+0.9}_{-0.7}$	$1.1^{+0.2}_{-0.2}$
221	16	ISIS	0.184	2.9	28.3	$26.6^{+0.4}_{-0.5}$	$25.0^{+0.2}_{-0.3}$	1.4	$1.67^{+0.21}_{-0.13}$	$1.0^{+0.5}_{-0.5}$	$1.3^{+0.2}_{-0.2}$
224	201 <sup>(25)</sup>	ISIS	1.547	1.0	$30.0^i$	$28.6^{+0.4}_{-0.4}$	$27.3^{+0.1}_{-0.2}$	1.8	$1.27^{+0.14}_{-0.11}$	$0.8^{+0.5}_{-0.4}$	$1.0^{+0.2}_{-0.2}$
236	5	FOS	0.473	2.6	29.2	$27.1^{+0.9}_{-1.0}$	$25.7^{+0.4}_{-0.1}$	0.7	$1.36^{+0.54}_{-0.42}$	$1.2^{+0.8}_{-0.8}$	$1.3^{+0.2}_{-0.3}$
236	21	ISIS	1.128	2.6	29.5	$28.2^{+1.1}_{-1.5}$	$26.7^{+0.3}_{-0.4}$	1.1	$1.47^{+0.43}_{-0.46}$	$0.8^{+1.1}_{-0.9}$	$1.1^{+0.3}_{-0.2}$
236	22	FOS	0.048	2.6	28.1	$25.1^{+0.7}_{-0.9}$	$23.7^{+0.5}_{-0.5}$	np	$1.34^{+0.31}_{-0.36}$	$1.8^{+0.7}_{-0.6}$	$1.7^{+0.3}_{-0.3}$
238	11	ISIS	0.325	4.1	28.3	$26.0^{+1.0}_{-1.8}$	$25.7^{+0.5}_{-0.4}$	1.9	$0.29^{+0.58}_{-0.67}$	$1.4^{+1.3}_{-0.8}$	$1.0^{+0.3}_{-0.3}$
245	4 <sup>(36)</sup>	ISIS	0.711	8.8	28.8	$27.5^{+1.1}_{-1.4}$	$26.2^{+0.3}_{-0.1}$	1.1	$1.33^{+0.55}_{-0.62}$	$0.7^{+1.1}_{-0.9}$	$1.0^{+0.1}_{-0.2}$
248	51	HB	0.242	1.5	29.8	$27.2^{+0.2}_{-0.2}$	$25.7^{+0.1}_{-0.1}$	—	$1.46^{+0.07}_{-0.05}$	$1.6^{+0.3}_{-0.3}$	$1.6^{+0.2}_{-0.2}$
252	1 <sup>(43)</sup>	ISIS	0.219	0.8	$27.7^i$	$26.1^{+0.4}_{-0.5}$	$25.4^{+0.2}_{-0.3}$	3.7	$0.71^{+0.17}_{-0.19}$	$1.0^{+0.5}_{-0.5}$	$0.9^{+0.2}_{-0.2}$
252	31**	HB	1.413	0.8	31.3	$29.2^{+0.1}_{-0.1}$	$28.1^{+0.1}_{-0.1}$	0.6	$1.15^{+0.03}_{-0.04}$	$1.3^{+0.3}_{-0.3}$	$1.2^{+0.1}_{-0.1}$
252	31**	HB	1.415	0.8	31.3	$29.2^{+0.1}_{-0.1}$	$28.1^{+0.1}_{-0.1}$	0.6	$1.15^{+0.03}_{-0.04}$	$1.3^{+0.3}_{-0.3}$	$1.2^{+0.1}_{-0.1}$
252	46	HB	2.091	0.8	30.9	$29.3^{+0.5}_{-0.5}$	$27.8^{+0.2}_{-0.2}$	—	$1.47^{+0.17}_{-0.10}$	$1.0^{+0.5}_{-0.5}$	$1.2^{+0.2}_{-0.2}$
255	7	ISIS	0.260	5.1	27.8	$26.5^{+1.1}_{-2.6}$	$25.2^{+0.8}_{-0.6}$	2.6	$1.22^{+0.66}_{-0.99}$	$0.8^{+1.8}_{-0.9}$	$1.0^{+0.3}_{-0.4}$
255	13	ISIS	0.581	5.1	29.1	$27.6^{+1.0}_{-1.6}$	$25.9^{+0.4}_{-0.4}$	0.1	$1.63^{+0.49}_{-0.53}$	$0.9^{+1.2}_{-0.8}$	$1.2^{+0.3}_{-0.3}$
255	23	ISIS	0.759	5.1	29.0	$27.4^{+1.3}_{-2.4}$	$26.4^{+0.4}_{-0.4}$	-0.2	$1.01^{+0.61}_{-0.83}$	$1.0^{+1.7}_{-1.0}$	$1.0^{+0.3}_{-0.3}$
257	37	ISIS	0.329	2.2	27.9	$26.4^{+0.7}_{-1.0}$	$25.4^{+0.4}_{-0.4}$	1.0 <sup>w</sup>	$1.05^{+0.31}_{-0.36}$	$0.9^{+0.8}_{-0.6}$	$1.0^{+0.3}_{-0.3}$
258	5	ISIS	0.811	3.4	29.2	$28.1^{+0.7}_{-0.8}$	$26.4^{+0.2}_{-0.2}$	1.2	$1.64^{+0.24}_{-0.26}$	$0.7^{+0.7}_{-0.6}$	$1.1^{+0.2}_{-0.2}$
258	30	ISIS	0.847	3.4	29.1	$24.6^u$	$26.4^u$	np	$-1.1^{+1.7}_{-1.4}$	$2.7^u$	$1.0^u$
259	30	HB	1.940	2.0	29.7	$27.7^{+0.9}_{-1.4}$	$27.6^{+0.2}_{-0.3}$	—	$0.15^{+0.35}_{-0.42}$	$1.2^{+1.1}_{-0.7}$	$0.8^{+0.2}_{-0.2}$

**Table 2** (continued): Optical/UV and X-ray continuum parameters.

FID	S No	Ins	z	$N_{\text{HGal}}$	$L_{2500}$	$L_{0.2\text{keV}}$	$L_{2\text{keV}}$	$\alpha_{\text{opt}}$	$\alpha_x$	$\alpha_{\text{os}}$	$\alpha_{\text{ox}}$
(1)	(2)	(3)	(4)	(5)	(6)	(7)	(8)	(9)	(10)	(11)	(12)
262	1	ISIS	0.882	3.4	29.4	$28.0^{+0.7}_{-0.8}$	$26.5^{+0.2}_{-0.2}$	0.5	$1.52^{+0.25}_{-0.28}$	$0.8^{+0.7}_{-0.6}$	$1.1^{+0.2}_{-0.2}$
262	2	HB	1.202	3.4	30.7	$28.2^{+0.6}_{-0.8}$	$27.0^{+0.2}_{-0.2}$	—	$1.16^{+0.25}_{-0.24}$	$1.5^{+0.7}_{-0.6}$	$1.4^{+0.2}_{-0.2}$
262	10	HB	0.336	3.4	29.8	$27.5^{+0.2}_{-0.2}$	$26.3^{+0.1}_{-0.1}$	—	$1.24^{+0.10}_{-0.08}$	$1.4^{+0.3}_{-0.3}$	$1.4^{+0.2}_{-0.2}$
262	12	IDS	0.923	3.4	29.5	$28.0^{+0.6}_{-0.6}$	$26.8^{+0.1}_{-0.2}$	$0.9^w$	$1.28^{+0.22}_{-0.21}$	$0.9^{+0.6}_{-0.5}$	$1.1^{+0.2}_{-0.2}$
262	34	IDS	0.311	3.4	29.0	$27.2^{+0.3}_{-0.4}$	$25.8^{+0.2}_{-0.2}$	$0.8^p$	$1.44^{+0.17}_{-0.11}$	$1.1^{+0.4}_{-0.4}$	$1.2^{+0.2}_{-0.2}$
272	8	ISIS	1.817	4.7	$29.8^i$	$29.1^{+1.2}_{-1.8}$	$27.5^{+0.3}_{-0.5}$	1.0	$1.54^{+0.43}_{-0.51}$	$0.4^{+1.3}_{-0.9}$	$0.9^{+0.3}_{-0.2}$
272	18	ISIS	0.604	4.7	29.6	$27.7^{+0.7}_{-1.0}$	$26.7^{+0.2}_{-0.2}$	0.4	$1.08^{+0.33}_{-0.39}$	$1.1^{+0.8}_{-0.6}$	$1.1^{+0.2}_{-0.2}$
272	28	ISIS	0.444	4.7	28.4	$27.5^{+0.7}_{-0.8}$	$26.0^{+0.3}_{-0.3}$	np	$1.46^{+0.30}_{-0.31}$	$0.5^{+0.7}_{-0.6}$	$0.9^{+0.2}_{-0.2}$
273	22	FOS	1.075	2.8	30.8	$28.9^{+1.2}_{-0.7}$	$26.7^{+0.3}_{-0.1}$	0.7	$2.15^{+0.31}_{-0.35}$	$1.2^{+0.6}_{-0.9}$	$1.6^{+0.1}_{-0.2}$
281	11	ISIS	2.919	5.8	30.1	$29.1^{+1.8}_{-3.1}$	$28.0^{+0.6}_{-1.0}$	1.8	$1.15^{+0.66}_{-0.79}$	$0.6^{+2.1}_{-1.3}$	$0.8^{+0.5}_{-0.3}$
281	21	IDS	0.347	5.8	28.5	$26.6^{+0.9}_{-1.2}$	$26.0^{+0.4}_{-0.2}$	2.4	$0.68^{+0.49}_{-0.57}$	$1.2^{+0.9}_{-0.8}$	$1.0^{+0.2}_{-0.3}$
283	11	FOS	0.272	10.	29.7	$24.9^{+1.0}_{-2.3}$	$25.7^{+0.7}_{-0.5}$	0.5	$-0.67^{+0.60}_{-0.77}$	$2.9^{+1.6}_{-0.8}$	$1.6^{+0.3}_{-0.4}$
283	21	IDS	0.719	10.	29.6	$26.1^{+1.0}_{-2.1}$	$26.5^{+0.4}_{-0.1}$	0.8	$-0.35^{+0.56}_{-0.69}$	$2.1^{+1.5}_{-0.8}$	$1.2^{+0.1}_{-0.3}$
293	1	ISIS	0.824	4.6	29.5	$27.5^{+1.1}_{-2.0}$	$26.7^{+0.2}_{-0.2}$	-0.8	$0.83^{+0.52}_{-0.71}$	$1.2^{+1.4}_{-0.9}$	$1.1^{+0.2}_{-0.2}$
293	6 <sup>(43)</sup>	FOS	0.081	4.6	29.4	$26.0^{+0.4}_{-0.5}$	$24.8^{+0.2}_{-0.2}$	2.9	$1.26^{+0.21}_{-0.22}$	$2.1^{+0.5}_{-0.4}$	$1.8^{+0.2}_{-0.2}$
293	12	IDS+ISIS	0.917	4.6	29.6	$27.3^{+1.5}_{-3.0}$	$26.7^{+0.3}_{-0.1}$	0.4	$0.68^{+0.85}_{-0.97}$	$1.4^{+2.0}_{-1.1}$	$1.1^{+0.1}_{-0.2}$
294	1	ISIS	0.713	4.3	29.2	$27.8^{+0.7}_{-0.8}$	$26.5^{+0.2}_{-0.2}$	np	$1.29^{+0.29}_{-0.30}$	$0.9^{+0.7}_{-0.6}$	$1.0^{+0.2}_{-0.2}$
302	14	IDS	0.809	1.2	29.7	$27.7^{+0.5}_{-0.5}$	$26.6^{+0.2}_{-0.2}$	0.6	$1.15^{+0.16}_{-0.17}$	$1.2^{+0.5}_{-0.5}$	$1.2^{+0.2}_{-0.2}$
302	18 <sup>(36)</sup>	ISIS	0.924	1.2	30.1	$27.7^{+0.4}_{-0.5}$	$27.0^{+0.1}_{-0.1}$	0.3	$0.75^{+0.14}_{-0.17}$	$1.5^{+0.5}_{-0.5}$	$1.2^{+0.2}_{-0.2}$
305	11	IDS	0.251	2.3	28.8	$27.1^{+0.3}_{-0.3}$	$25.7^{+0.2}_{-0.2}$	0.9	$1.44^{+0.13}_{-0.10}$	$1.0^{+0.4}_{-0.4}$	$1.2^{+0.2}_{-0.2}$
305	18 <sup>(39)</sup>	IDS	0.387	2.3	28.8	$26.4^{+0.6}_{-0.8}$	$26.1^{+0.2}_{-0.2}$	1.1	$0.28^{+0.27}_{-0.31}$	$1.5^{+0.7}_{-0.5}$	$1.0^{+0.2}_{-0.2}$
305	34 <sup>(46)</sup>	IDS	0.854	2.3	29.8	$27.8^{+0.6}_{-0.7}$	$26.7^{+0.2}_{-0.2}$	-0.3	$1.06^{+0.21}_{-0.23}$	$1.3^{+0.6}_{-0.6}$	$1.2^{+0.2}_{-0.2}$

Sample statistics (includes data from Paper I)

	z	$N_{\text{HGal}}$	$L_{2500}$	$L_{0.2\text{keV}}$	$L_{2\text{keV}}$	$\alpha_{\text{opt}}$	$\alpha_x$	$\alpha_{\text{os}}$	$\alpha_{\text{ox}}$	
median		0.719	2.3	29.3	27.6	26.5	0.8	1.08	1.1	1.12
mean		0.82	2.8	30.2	28.2	27.0	0.9	1.07	1.4	1.16
$\sigma$		0.53	1.9	0.6	0.5	0.5	0.9	0.51	0.6	0.18
error		0.04	0.2	0.1	0.1	0.1	0.1	0.04	0.1	0.02

(1) RIXOS field number (see Mason et al, in preparation); (2) RIXOS source number (Mason et al, in preparation) - the number in brackets is the radius of the extraction circle used for the X-ray data (in arcseconds) where it is less than 54 arcsec (see Paper I); (3) the instrument with which the spectrum was taken - see Section 2.2; HB - Hewitt & Burbridge (1989; spectrum not taken); MSS - Gioia et al. (1984; spectrum not taken) (4) redshift; (5) Galactic column density ( $10^{20} \text{ cm}^{-2}$ ) - errors are  $\sim 10$  per cent (see also Paper I); (6) log of the monochromatic UV luminosity at 2500 Å ( $\text{erg s}^{-1} \text{ Hz}^{-1}$ ) - error is estimated to be  $\sim 50$  percent (Section 2.2.1); (7) log of the monochromatic X-ray luminosity at 0.2 keV ( $\text{erg s}^{-1} \text{ Hz}^{-1}$ ) - errors are calculated from the 90% errors on the fits (Paper I); (8) log of the monochromatic X-ray luminosity at 2.0 keV ( $\text{erg s}^{-1} \text{ Hz}^{-1}$ ) - errors are calculated from the 90% errors on the fits (Paper I); (9) energy index of the best-fitting power-law to the optical/UV continuum - error is estimated to be  $\pm 0.5$  (Paper I); (10) energy index of the best-fitting power-law to the X-ray data - errors are 90% (Paper I); (11) and (12) for definitions see Section 2.3 - errors are calculated from the quoted errors on  $L_{2500}$ ,  $L_{0.2\text{keV}}$  and  $L_{2\text{keV}}$ ;  $i$  - CCD image taken;  $w$  - optical/UV continuum weak;  $p$  optical/UV power-law slope poor fit;  $u$  X-ray power-law slope poor fit, data uncertain; np - spectrum not taken at the parallactic angle; \* F212\_32 is a double quasar; the optical data have been measured from spectra of the individual components, but the components are not resolved in the PSPC image, thus  $\alpha_x$  is the slope for the total X-ray emission while the  $L_{0.2\text{keV}}$  and  $L_{2\text{keV}}$  for each component comprise one half of the total; \*\* F252\_31 is the double quasar E0957+561; the optical spectrum of only one component (from Puchnarewicz et al. 1992) was available and this was assumed to be the same for both. The components are not resolved in the X-ray image, thus  $\alpha_x$  is the slope for the total X-ray emission while the  $L_{0.2\text{keV}}$  and  $L_{2\text{keV}}$  for each component comprise one half of the total. The median, mean,  $\sigma$  (i.e. standard deviation on the mean) and error on the mean have been calculated for the full sample used (excluding uncertain parameters), i.e. including those whose continuum parameters are given in Paper I.

second-order polynomial in the fits. The FWHM of the lines are the FWHM of the best-fitting Gaussian model, while fluxes and EWs were measured directly from the spectrum after the fitted continuum and Gaussian model fluxes of any other contaminants had been subtracted. The FWHM have

been deconvolved from the instrumental width.

Line luminosities were calculated assuming a value of  $50 \text{ km s}^{-1} \text{ Mpc}^{-1}$  for the Hubble constant ( $H_0$ ) and 0 for the deceleration parameter ( $q_0$ ; these values are assumed throughout this paper). Luminosities of sources for which

CCD data were also available, were explicitly corrected for any light lost around the slit; the remaining luminosities were increased by the mean correction factor of 1.2 (see Section 2.2). Line EWs, FWHM and luminosities are given in Table 1.

In some cases, two Gaussian components were required to fit the profile of the permitted lines and data for the separate fits are given in Table 1. For the optical lines (i.e. H $\alpha$  and H $\beta$ ), these have been assumed to represent emission from the broad and narrow line regions and are indicated ‘b’ and ‘n’ respectively in the table. For the UV lines (MgII and CIII]), an additional ‘very broad’ underlying component with a FWHM of  $\sim 10000$  km s $^{-1}$  was sometimes observed; these are also given in Table 1 and indicated ‘v’ (the lower velocity component for the UV lines is assumed to come from the ‘normal’ BLR and is tagged ‘b’).

A particular problem in the measurement of emission-line parameters is that of line and continuum blending. Blends of FeII can be strong throughout the optical and UV and especially around H $\beta$ , [OIII] and MgII. Modelling of the FeII such as that of Wills, Netzer & Wills (1985), has been used by previous authors to both measure the FeII blends themselves and to remove the FeII features before measuring residual line and continuum features. Although we have not used such techniques here (as these require data with a very high signal to noise ratio), obvious blends around the H $\beta$ /[OIII] and MgII regions have been removed in the fitting procedure before measuring the lines. The CIII] line is often blended with AlIII $\lambda 1857$  and SiIII $\lambda 1892$ ; Steidel & Sargent (1991) found that AlIII $\lambda 1857$  may contribute up to 12 percent of the flux attributed to CIII], while the SiIII $\lambda 1892$  component is not significant. The quality of the RIXOS spectra do not permit the reliable deblending of these features and we caution the reader of possible contamination in the line parameters presented here.

Balmer continuum and optical FeII emission can also blend to produce a “quasi”-continuum at around 3000 Å (Wills et al. 1985) and this may affect measurements of the optical/UV spectral slope,  $\alpha_{\text{opt}}$ . This has been reduced by removing all absorption and emission features and regions with a very low signal-to-noise ratio before measuring  $\alpha_{\text{opt}}$ . By also using the broadest wavelength range available ( $\sim 5000$  Å in the observer-frame), we have ensured that contamination in  $\alpha_{\text{opt}}$  by the FeII/Balmer continuum has been minimized, although it may still affect AGN with very low- $z$ , or with  $z \sim 1.9$ , where the Balmer continuum region falls at the extremes of the observed spectra.

#### Errors and upper limits

Errors on the fluxes, EWs and FWHM have been estimated by comparing parameters from repeated observations of the same AGN (i.e. to assess systematic errors) and by repeating measurements on the same spectrum (to assess uncertainties induced by the fitting techniques by, for example, the allowed extremes in continuum level). Typical errors are  $\pm 0.3$  on the logarithm of the luminosity,  $\pm 0.3$  on the logarithm of the EW and  $\pm 0.15$  on the logarithm of the FWHM (except at FWHM- $< 2000$  km s $^{-1}$  which are less certain and have errors of  $\sim \pm 0.25$  dex). Parameters with larger errors than these are indicated by the superscript ‘u’ in Table 1 (i.e. the value quoted is uncertain). Possible problems with the subtraction of contaminating FeII and/or the

Balmer continuum will add to the uncertainties. Also, additional errors should be considered on the logarithm of the line luminosities when individual lines are compared with the X-ray parameters as these have been taken at a different epoch. The magnitude of such errors are difficult to quantify but, for example, the X-ray spectra of many AGN typically show flux variability of  $\sim \pm 50$  per cent (Mushotzky, Done & Pounds 1993; Nicholson, Mittaz & Mason 1997). While these errors are relatively high, the large number of AGN should allow a meaningful sample analysis to be made nonetheless.

Upper limits on line fluxes and EWs were calculated from the parameters of a Gaussian profile which was judged by eye to overestimate the emission from a ‘true’ line. The position of the Gaussian was fixed at the expected position of the line; the FWHM for upper limits on permitted lines was fixed to the width of the strongest permitted line detected in the same spectrum, while for [OIII] it was fixed at 1000 km s $^{-1}$ . Upper limits on EWs and luminosities are indicated by ‘l’ in Table 1; fixed FWHM are indicated by ‘f’.

### 2.3 Continuum slopes and luminosities

The optical and X-ray continuum parameters of many AGN used in this sample have already been presented in Paper I, to which we refer the reader. Slopes and luminosities for objects not covered by Paper I are listed here in Table 2, and have been derived in an identical manner. All power-law indices or slopes,  $\alpha$ , have been defined such that  $F_\nu \propto \nu^{-\alpha}$ .

We shall be describing much of the changes observed in the RIXOS optical and X-ray spectra in terms of the gradients of the continuum slopes. Different terminologies are commonly used in the literature for the slopes in the optical and the X-ray ranges, thus to avoid any confusion, we have adopted a single convention for both, i.e. using the terms “soft” and “hard”. A “soft” slope falls towards high energies and has a relatively high energy index  $\alpha$  (recalling here that the negative sign is implicit in our definition of  $\alpha$ ); in the optical region, a soft slope corresponds to a “red” continuum. A “hard” slope rises towards high energy and has a low or negative  $\alpha$ ; this corresponds to a “blue” slope in the optical. To describe changes in slope, we will use the terms “soften” (i.e.  $\alpha$  increasing) and “harden” (where  $\alpha$  is decreasing).

#### 2.3.1 Optical

The logarithms of the UV and optical continuum luminosities in the quasar rest-frame at 2500 Å and 5000 Å ( $L_{2500}$  and  $L_{5000}$  respectively) were calculated from the best-fitting power-law model fits to the spectra. Luminosities of sources for which CCD data were also available were explicitly corrected for any light lost around the slit; the remaining luminosities were increased by the mean correction factor of 1.2 (see Section 2.2). While  $L_{5000}$  is only measured where the rest-frame flux at 5000 Å falls within the observed wavelength range,  $L_{2500}$  has been extrapolated where necessary from the power-law fits. Taking into account possible variability, light losses around the slit and errors on the power-law fits, we estimate that uncertainties on the logarithm of the optical and UV luminosities are typically  $\sim \pm 0.3$ .

### 2.3.2 X-ray

The PSPC counts were divided into three bands [0.1 to 0.4 keV (channels 8 to 41); 0.5 to 0.9 keV (channels 52 to 90) and 0.9 to 2.0 keV (channels 91 to 201)] and these were combined to produce ‘spectra’ with three data points for each source. The spectra were fitted with single power-law models using the method described in Mittaz et al. (1997), which finds the best-fit by minimizing a Poissonian-based statistic. In the fits, the absorbing column density was fixed at the Galactic column ( $N_{\text{H,Gal}}$ ) measured from the 21 cm survey of Stark et al. (1992). All instrumental effects, including vignetting, dead-time corrections and particle contamination, were folded into the fitting process. Mittaz et al. (1997) have demonstrated that this model provides a good fit to the data, reproducing the observed X-ray colours to within  $1\sigma$  in more than 90 percent of cases, and within  $3\sigma$  for all AGN.

The logarithms of the X-ray luminosities at 0.2 keV ( $L_{0.2\text{keV}}$ ) and 2 keV ( $L_{2\text{keV}}$ ) in  $\text{ergs s}^{-1} \text{Hz}^{-1}$  in the rest-frame of the quasar were calculated using the best-fit power-law model for each individual source. The ratios of UV (i.e.  $L_{2500}$ ) to X-ray luminosity at 2.0 keV and 0.2 keV are parameterized using  $\alpha_{\text{ox}}$  (Tananbaum et al. 1979) and  $\alpha_{\text{os}}$  (Puchnarewicz et al. 1992) respectively. X-ray luminosities, power-law indices,  $\alpha_{\text{ox}}$ ,  $\alpha_{\text{os}}$  and their 90% errors are given in Table 2 and Paper I.

## 3 PROPERTIES OF THE RIXOS AGN SAMPLE

Number distributions of all optical and UV emission line parameters for the RIXOS AGN (except the [OIII] FWHM which are unresolved) are plotted in Figs 1 and 2, while the distributions of redshift and of the optical/UV and X-ray continuum parameters are plotted in Fig 3. The median, mean,  $\sigma$  (i.e. standard deviation on the mean) and error on the mean for all continuum and emission line parameters are given in Tables 1 and 2. Uncertain parameters (see Tables 1 and 2) were excluded from the distributions shown and the sample statistics; source number 6 in field 273 was also excluded because of its unusual nature (see section 4.5.1). Upper limits have not been taken into account. For the permitted lines where two components were fitted to the profile, only the ‘broad’ components were included in these calculations. Further details of the continuum properties for the RIXOS AGN may be found in Paper I.

### 3.1 Balmer lines

The mean  $\text{H}\alpha$  EW for the RIXOS AGN is  $140 \pm 20 \text{ \AA}$  (the error quoted is the standard error on the mean) which is lower than that which we calculate for the Stephens (1989) sample of brighter X-ray selected AGN (i.e.  $233 \pm 23 \text{ \AA}$ ; see Fig 1). The mean  $\text{H}\alpha$  FWHM of the RIXOS AGN is  $3100 \pm 400 \text{ km s}^{-1}$ .

The mean RIXOS  $\text{H}\beta$  EW is  $38 \pm 3 \text{ \AA}$ , which like  $\text{H}\alpha$ , is lower than that which we calculate for the Stephens (1989) sample (a mean of  $77 \pm 7 \text{ \AA}$ ). It is also lower than the mean for the optically-selected Boroson & Green (1992; hereafter BG) sample;  $96 \pm 4 \text{ \AA}$  (see Fig 1). Goodrich (1989) also noted that the  $\text{H}\beta$  EWs of X-ray selected AGN were lower than those of optically-selected objects and suggested that this

was related to the X-ray flux.

The mean  $\text{H}\beta$  FWHM is  $3900 \pm 400 \text{ km s}^{-1}$  (excluding objects with poorly determined broad components; these are indicated with the superscript  $u$  in Table 1). This is similar to the mean for the BG sample, which we calculate to be  $3800 \pm 200 \text{ km s}^{-1}$  (see Fig 1), and suggests that although the  $\text{H}\beta$  emission is weak relative to the optical continuum, the velocity of the BLRs in the RIXOS AGN may be comparable to those of optically-selected AGN (although the  $\text{H}\beta$  FWHM may be lowered by the effects of absorption in the RIXOS AGN; see Section 4.5). The mean for the Stephens sample is  $3200 \pm 200 \text{ km s}^{-1}$ , which is also similar to that of the RIXOS AGN.

### 3.2 [OIII]

The mean EW of the [OIII] emission in the RIXOS AGN is  $29 \pm 3 \text{ \AA}$ ; this is similar to BG and slightly lower than Stephens which have mean [OIII] EWs of  $24 \pm 3 \text{ \AA}$  and  $44 \pm 8 \text{ \AA}$  respectively. All three samples are compared in Fig 1 and show very similar distributions. (The [OIII] lines were unresolved in most cases thus their FWHM distribution and mean properties have not been given.)

The similarity of the RIXOS AGN [OIII] EW distribution to the BG sample (which are UV-excess selected and thus presumably relatively unobscured) is a surprising result, if indeed the RIXOS sample suffers the effects of dust absorption (Paper I). If the absorption occurs between the BLR and the NLR, perhaps in a molecular torus, then while the [OIII] luminosity would be unaffected, the optical continuum would be absorbed, leading to generally higher values of the [OIII] EW in absorbed objects (see also Section 5.3). The presence of an absorbing medium between the BLR and NLR which modifies the optical continuum, was also suggested by Baker (1997) for her sample of radio-loud quasars. However, relatively high [OIII] EWs are not seen in the absorbed (i.e. RIXOS) objects when compared with the unobscured (i.e. BG quasars).

We have estimated the effect that absorption would have on the [OIII] EW distribution of the RIXOS AGN, using the X-ray continuum slope as a ‘measurement’ of the cold gas absorption and assuming a Galactic gas-to-dust ratio [i.e. where an  $E(B-V)$  of 1 corresponds to  $N_{\text{H}} = 6 \times 10^{21} \text{ cm}^{-2}$ ; Ryter, Cesarsky & Audouze 1975; Gorenstein 1975]. Using the  $\alpha_{\text{x}}$  and redshift of each individual AGN, the cold gas column density was interpolated from the model curves shown in Figure 17 of Paper I. By assuming that all objects have an [OIII] EW of  $25 \text{ \AA}$  when unaffected by absorption (i.e. similar to the BG mean), then using the reddening curves of Cardelli, Clayton & Mathis (1989), we find that the mean [OIII] EW of the RIXOS AGN would be  $\sim 63 \text{ \AA}$ ; significantly higher than that which we observe.

This cannot be due to a relatively strong optical continuum in the RIXOS AGN; the mean absolute V-band magnitude of the BG sample is  $-24.2 \pm 0.2$ , whereas for the RIXOS objects with measured [OIII], the mean is  $-21.3 \pm 0.2$ , i.e. an order of magnitude fainter. Instead it may be that the [OIII] line luminosity is itself relatively low in the RIXOS AGN. Since the  $\text{H}\beta$  and  $\text{H}\alpha$  EWs also appear to be weak relative to the BG sample (Section 3.1; EWs of lines emitted from within the absorber will be unaffected if the continuum also comes from within), this suggests either that the ionizing

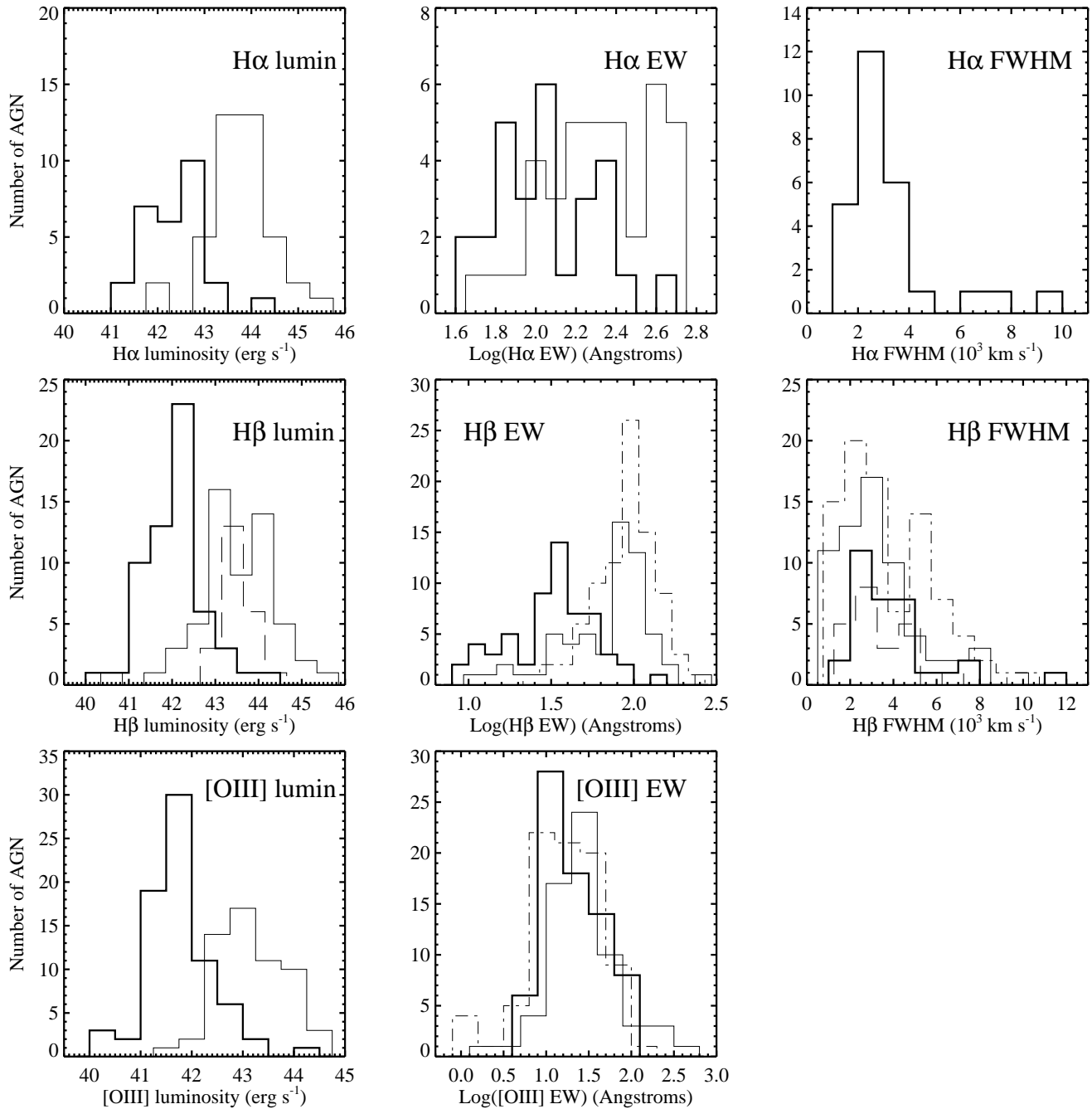


**Figure 1.** Number distributions of the optical emission line parameters for the RIXOS AGN, including luminosities, EWs and FWHM of  $H\alpha$ ,  $H\beta$  and  $[OIII]$ . Other samples have also been plotted for comparison: the Stephens (1989) data ( $L_{H\alpha}$ ,  $H\alpha$  EW,  $L_{H\beta}$ ,  $H\beta$  EW,  $H\beta$  FWHM,  $L_{[OIII]}$  and  $[OIII]$  EW) are drawn with a thin, solid line; the Boroson & Green (1992) data ( $H\beta$  EW,  $H\beta$  FWHM and  $[OIII]$  EW) are drawn with a dot-dashed line; and the Laor et al. (1997) data ( $L_{H\beta}$  and  $H\beta$  FWHM) are plotted with a long-dashed line.

flux on the Balmer line region and the NLR is relatively low, or that the covering factors of these regions are low.

### 3.3 MgII and CIII]

The mean MgII EWs and FWHM for the RIXOS AGN are  $37 \pm 3$  Å and  $4600 \pm 200$  km s $^{-1}$  respectively. The mean EW is similar to that which we calculate for the Steidel & Sargent (1991; hereafter SS91) sample of radio-loud and radio-quiet

objects ( $34 \pm 2$  Å). The mean FWHM is similar to that of Brotherton et al. (1994; hereafter B94) who found a mean of  $4440 \pm 200$  km s $^{-1}$  (the B94 sample is drawn from SS91). Thus there appears to be no overall differences in the EWs and FWHM of the MgII line, compared with the general AGN population (this is also borne out in Fig 2).

The mean CIII] EW for the RIXOS AGN is  $22 \pm 3$  Å; this is similar to those of the Green (1996) sample ( $16.5 \pm 1.9$  Å) and the SS91 sample ( $18.2 \pm 0.7$  Å; see Fig 2). The mean

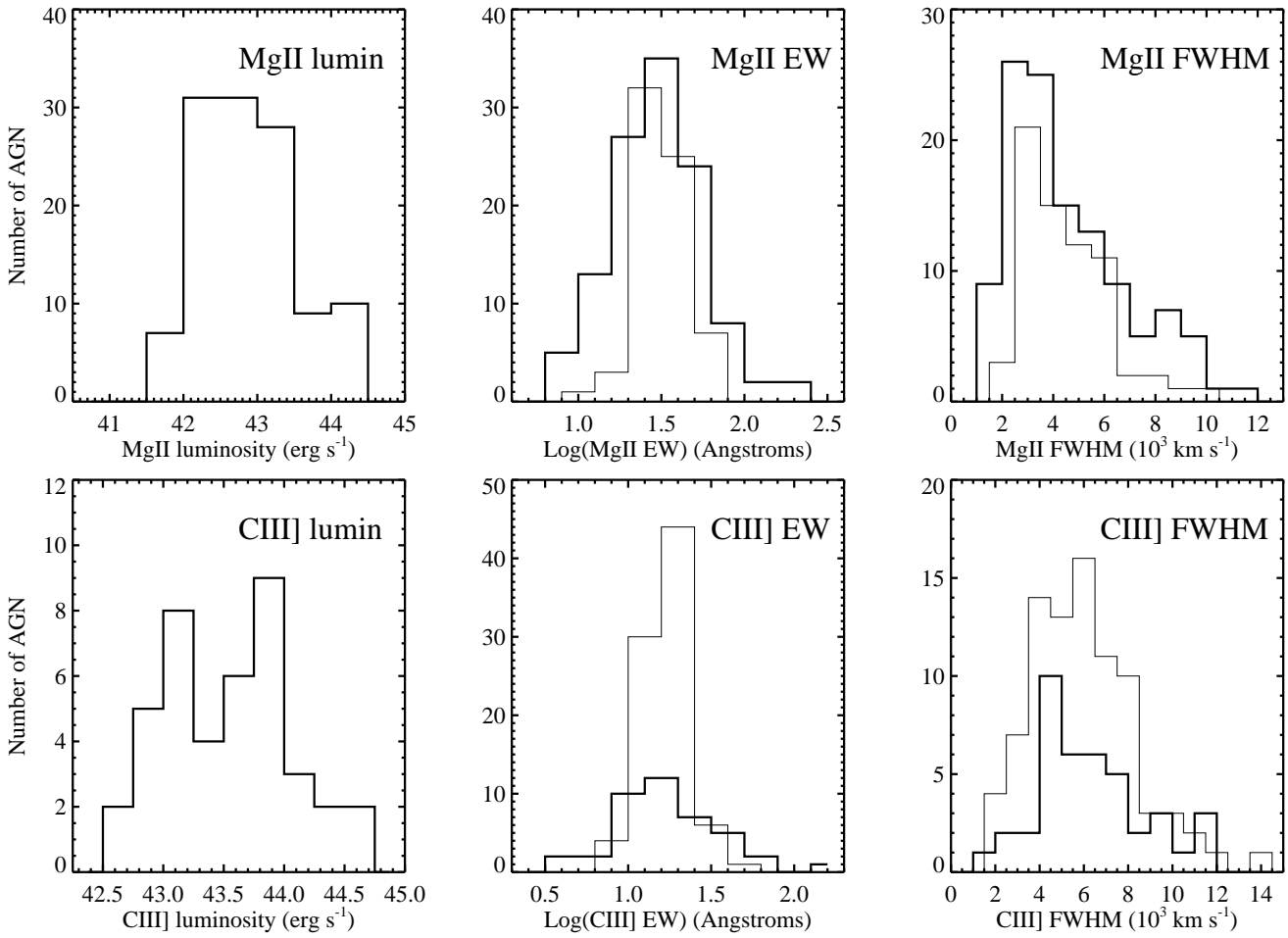


**Figure 2.** Number distributions of the UV emission line parameters for the RIXOS AGN (drawn as a thick histogram), including luminosities, EWs and FWHM of MgII and CIII]. The data from Steidel & Sargent (1991) and Brotherton et al. (1994) are also drawn for comparison as thin lines.

FWHM of the CIII] emission in the RIXOS AGN is  $6300 \pm 400 \text{ km s}^{-1}$  which is similar to that of the radio-quiet objects in the B94 sample ( $6880 \pm 340 \text{ km s}^{-1}$ ; the mean CIII] FWHM of the radio-loud AGN in the B94 sample was significantly lower, i.e.  $4990 \pm 310 \text{ km s}^{-1}$ ) and to the UV-bright sample of Green (1996) where the mean CIII] FWHM was  $6340 \pm 520 \text{ km s}^{-1}$ . Like MgII then, the CIII] strengths and widths are similar to the AGN population as a whole.

#### 4 CORRELATIONS

In this section, we search for relationships between the various line and continuum parameters, using the Spearman rank-order correlation coefficient which is a non-parametric method insensitive to outlying points. Results of the correlation analysis between line parameters and continuum slopes and luminosities are given in Table 3, while correlations between line EWs, luminosities and FWHM are listed in Tables 4a and b. Correlations for the continuum parameters only, are presented in Paper I; although we have used a slightly different sample of objects to that in Paper I, the correlations between the continuum parameters for the AGN in Paper I are consistent with the sample used here.

The ‘correlation probabilities’,  $p_{\text{corr}}$ , which are given in the following sections and in the tables, are expressed as percentages and are equal to 100% minus the percentage probability of being drawn from a random sample. Neither uncertain line parameters, upper limits nor data for double quasars have been included in the correlations. In general the number of upper limits represents only 7 per cent of the line parameters, thus their exclusion will have a small effect on the correlation analysis. The emission line with the largest fraction of upper limits (15 per cent) is H $\beta$ ; in this case the effect of including upper limits or uncertain values are considered where appropriate. Also excluded were (1) data taken from the literature; (2) weak optical continua or optical continua which were poorly fitted by a simple power-law model; and (3) X-ray data for sources which lay less than 30 arcseconds away from a neighbouring X-ray source. Where two components are given for the emission lines in Table 1, only the broad components (i.e. those indicated *b* in Table 1) have been used.

One problem in searching for correlations in flux-limited samples of this kind, is that luminosities are dominated by the correction for the distance to the quasar, so that the lines and continua of low-redshift objects have low lumi-

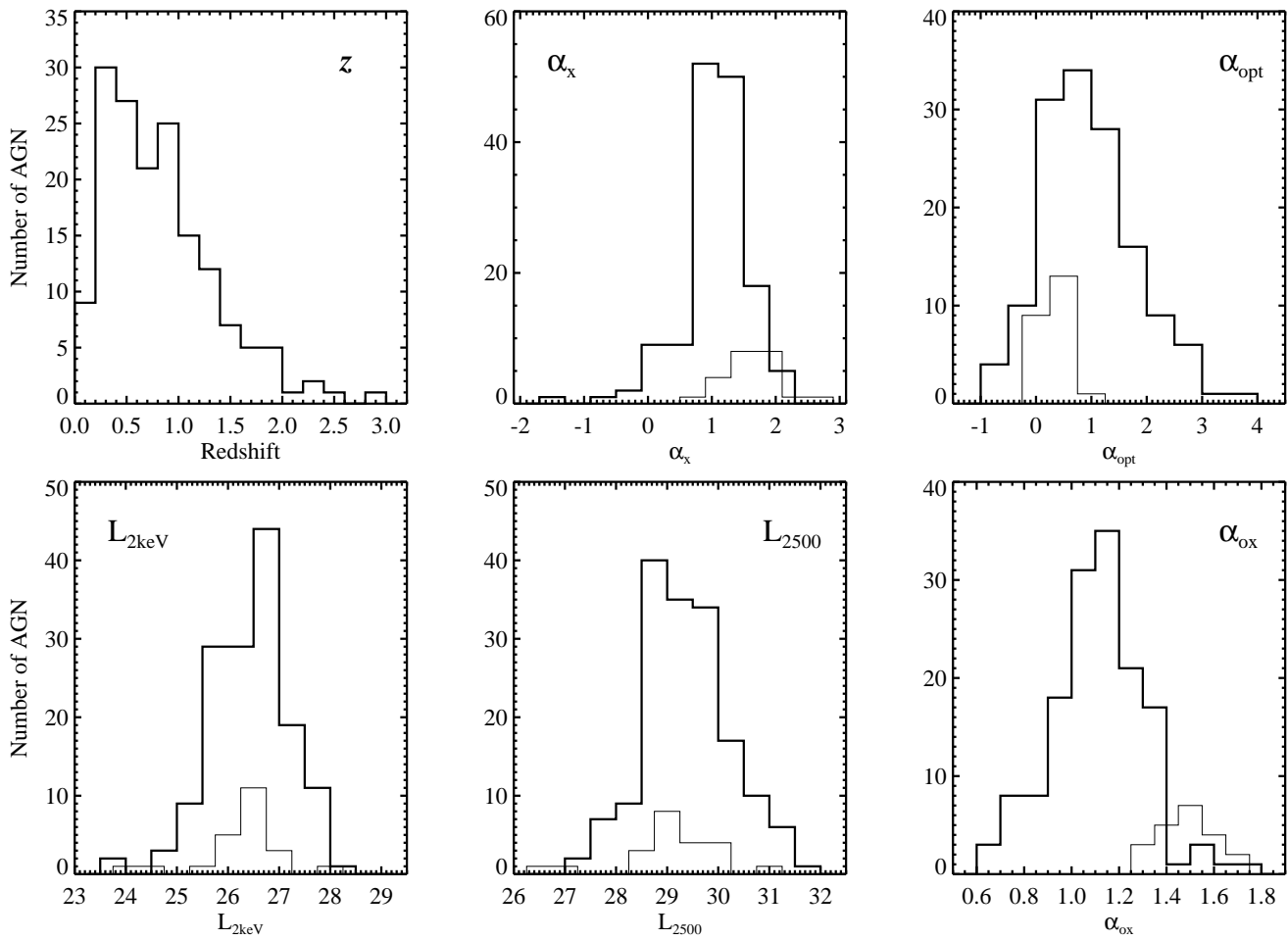


**Figure 3.** Number distributions of optical/UV and X-ray continuum parameters for the RIXOS AGN, including redshift, X-ray and optical/UV power-law slopes ( $\alpha_x$  and  $\alpha_{\text{opt}}$ ), X-ray and UV continuum luminosities ( $L_{2\text{keV}}$  and  $L_{2500}$ ) and  $\alpha_{\text{ox}}$ . Histograms for the RIXOS AGN are drawn as thick histograms; also plotted as thin histograms are the distributions for the Laor et al. (1997) sample.

nosities while parameters of high- $z$  objects tend to have high luminosities. This usually results in very strong correlations between luminosities of different parameters (lines and continua) and may not reflect a real dependence. In order to correct for this, when comparing parameters which are both luminosities, each pair of parameters is divided by a factor which is appropriate to the redshift of that object. The factor used is the rest-frame luminosity calculated for a flux of  $1 \times 10^{-15}$  ergs  $\text{cm}^{-2}$   $\text{s}^{-1}$  measured in the frame of the observer (arbitrarily chosen to match the observed-flux typically measured in the optical emission lines).

When comparing optical/UV properties with X-ray parameters, it must be borne in mind that these optical data are not simultaneous with the X-ray observations and the optical data are not photometric, although efforts have been made to correct for this (see Section 2.2). While these effects should average out over the large sample used here, they will introduce an additional degree of scatter into quantities such as  $\alpha_{\text{ox}}$  which are calculated from both optical and X-ray spectra. Correlations between separate optical/UV and X-ray parameters may also have an additional element of scatter for these reasons.

#### 4.1 Continuum luminosities

All emission line luminosities are strongly correlated (>99 per cent) with the optical/UV continuum luminosities,  $L_{5000}$  and  $L_{2500}$ . The  $\text{H}\beta$ ,  $[\text{OIII}]$  and  $\text{MgII}$  luminosities are also strongly correlated with  $L_{2\text{keV}}$  (>99 per cent); there is a weaker (98 per cent) correlation for  $\text{CIII}$  but for  $\text{H}\alpha$ , the  $p_{\text{corr}}$  with  $L_{2\text{keV}}$  is only 88 per cent. Correlations between the  $\text{H}\beta$  luminosity and the optical/UV and X-ray continuum luminosities have been reported in previous samples (e.g. Kriss & Canizares 1982; Blumenthal, Keel & Miller 1982; Stephens 1989, Laor et al. 1997).

There are weak correlations between the  $\text{H}\beta$  and  $\text{MgII}$  luminosities and the soft X-rays at 0.2 keV ( $p_{\text{corr}}=98$  per cent). However these may be induced; for example, looking at the subsample for which  $\text{MgII}$  has been measured, strong correlations are found in  $L_{\text{MgII}}$  versus  $L_{2\text{keV}}$ , and in  $L_{\text{MgII}}$  versus  $L_{2500}$ . For the same subsample,  $L_{0.2\text{keV}}$  is also related to  $L_{2\text{keV}}$  and  $L_{2500}$ , thus it is possible that the  $L_{\text{MgII}}$  versus  $L_{0.2\text{keV}}$  correlation is induced. The correlation between  $L_{\text{H}\beta}$  and  $L_{0.2\text{keV}}$  may be similarly affected. In contrast, for AGN with coverage of  $\text{H}\alpha$ , the continuum luminosities  $L_{2\text{keV}}$  and  $L_{5000}$  are not correlated with  $L_{0.2\text{keV}}$ ; neither is there a

**Table 3.** Emission line and continuum correlation probabilities  $[(r_S), p_{\text{corr}}]$ 

	$L_{5000}$ ( $r_S$ )	$L_{2500}$ ( $r_S$ )	$L_{0.2\text{keV}}$ ( $r_S$ )	$L_{2\text{keV}}$ ( $r_S$ )	$\alpha_{\text{opt}}$ ( $r_S$ )	$\alpha_x$ ( $r_S$ )	$\alpha_{\text{os}}$ ( $r_S$ )	$\alpha_{\text{ox}}$ ( $r_S$ )
$L_{\text{H}\alpha}$	(0.9) >99	(0.9) >99	(0.4) 59	(0.5) 88	(-0.5) 84	(0.1) 1	(0.2) 1	(0.0) 1
$L_{\text{H}\beta}$	(0.9) >99	(0.8) >99	(0.4) 97	(0.5) >99	(-0.4) 98	(0.1) 1	(0.1) 1	(0.2) 36
$L_{[\text{OIII}]}$	(0.7) >99	(0.6) >99	(0.2) 39	(0.5) >99	(-0.4) 98	(-0.1) 1	(0.2) 3	(0.1) 1
$L_{\text{MgII}}$	(0.7) >99	(0.7) >99	(0.3) 97	(0.5) >99	(-0.1) 1	(-0.1) 1	(0.3) >99	(0.3) 96
$L_{\text{CIII]}}$	(—) —	(0.9) >99	(0.3) 68	(0.5) 98	(0.2) 1	(0.0) 1	(0.4) 91	(0.6) >99
$\text{H}\alpha$ EW	(0.4) 62	(0.4) 59	(0.4) 54	(0.7) >99	(-0.2) 1	(-0.1) 1	(-0.1) 1	(-0.5) 84
$\text{H}\beta$ EW	(0.3) 47	(0.4) 94	(0.3) 91	(0.3) 55	(-0.4) 88	(0.1) 1	(0.0) 1	(0.1) 1
$[\text{OIII}]$ EW	(-0.1) 1	(-0.1) 1	(-0.1) 1	(0.2) 1	(0.0) 1	(-0.2) 16	(-0.1) 1	(-0.3) 95
$\text{MgII}$ EW	(-0.4) 95	(-0.5) >99	(-0.4) >99	(-0.2) 79	(0.1) 1	(-0.2) 89	(-0.2) 56	(-0.5) >99
$\text{CIII]}$ EW	(—) —	(-0.5) 98	(-0.3) 34	(-0.2) 1	(0.3) 52	(-0.1) 1	(-0.2) 1	(-0.4) 89
$\text{H}\alpha$ FWHM	(0.1) 1	(0.1) 1	(-0.1) 1	(0.4) 53	(0.1) 1	(-0.5) 91	(0.3) 8	(-0.2) 1
$\text{H}\beta$ FWHM	(0.3) 19	(0.5) 94	(0.2) 1	(0.4) 67	(-0.6) 99	(-0.2) 1	(0.1) 1	(0.1) 1
$\text{MgII}$ FWHM	(-0.3) 74	(0.0) 1	(0.0) 1	(0.1) 1	(0.1) 1	(-0.2) 52	(0.0) 1	(-0.2) 67
$\text{CIII]}$ FWHM	(—) —	(0.0) 1	(0.3) 26	(0.0) 1	(-0.1) 1	(0.3) 38	(-0.1) 1	(0.1) 1

The two quantities given for each correlation are the Spearman correlation coefficient ( $r_S$ , shown in brackets) and  $p_{\text{corr}}$ . Correlation coefficients between two different luminosities were calculated after having corrected for redshift (see Section 4). Percentages are not given where there were fewer than 7 data pairs. The  $[\text{OIII}]$  lines are unresolved thus correlations of the  $[\text{OIII}]$  FWHM with other data have not been made.

**Table 4a** Emission line correlation probabilities; luminosities and EWs correlated with luminosities, EWs and FWHM  $[(r_S), p_{\text{corr}}]$ .

	$L_{\text{H}\alpha}$ ( $r_S$ )	$L_{\text{H}\beta}$ ( $r_S$ )	$L_{[\text{OIII}]}$ ( $r_S$ )	$L_{\text{MgII}}$ ( $r_S$ )	$L_{\text{CIII]}}$ ( $r_S$ )	$\text{H}\alpha$ EW ( $r_S$ )	$\text{H}\beta$ EW ( $r_S$ )	$[\text{OIII}]$ EW ( $r_S$ )	$\text{MgII}$ EW ( $r_S$ )	$\text{CIII]}$ EW ( $r_S$ )
$L_{\text{H}\beta}$	(0.8) >99									
$L_{[\text{OIII}]}$	(0.8) >99	(0.6) >99								
$L_{\text{MgII}}$	(0.6) 57	(0.8) >99	(0.6) >99							
$L_{\text{CIII]}}$	(—) —	(—) —	(—) —	(—) —	(0.8) >99					
$\text{H}\alpha$ EW	(0.7) >99	(0.5) 87	(0.6) 98	(0.1) 17	(—) —					
$\text{H}\beta$ EW	(0.4) 67	(0.7) >99	(0.3) 61	(0.3) 25	(—) —	(0.5) 91				
$[\text{OIII}]$ EW	(0.1) 1	(-0.1) 1	(0.5) >99	(0.0) 1	(—) —	(0.4) 84	(0.1) 1			
$\text{MgII}$ EW	(0.6) 62	(-0.2) 1	(-0.1) 1	(-0.1) 1	(-0.3) 69	(0.6) 62	(-0.2) 1	(0.2) 1		
$\text{CIII]}$ EW	(—) —	(—) —	(—) —	(-0.3) 41	(-0.1) 1	(—) —	(—) —	(—) —	(0.5) 96	
$\text{H}\alpha$ FWHM	(0.3) 7	(0.2) 1	(0.0) 1	(-0.7) 75	(—) —	(0.5) 86	(0.1) 1	(-0.1) 1	(0.2) 21	(—) —
$\text{H}\beta$ FWHM	(0.9) 99	(0.4) 86	(0.1) 1	(0.3) 9	(—) —	(0.8) 99	(0.3) 57	(-0.2) 1	(0.5) 79	(—) —
$\text{MgII}$ FWHM	(-0.4) 37	(0.0) 1	(-0.1) 1	(0.3) 96	(0.0) 1	(—) —	(0.0) 1	(0.0) 1	(0.6) >99	(0.1) 1
$\text{CIII]}$ FWHM	(—) —	(—) —	(—) —	(0.1) 1	(0.2) 1	(—) —	(—) —	(—) —	(0.2) 12	(0.2) 1

Coefficients and probabilities between two different luminosities have been calculated after correction for redshift (see Section 4). Percentages are not given where there were fewer than 7 data pairs.

**Table 4b** Emission line correlation probabilities; FWHM correlated with FWHM  $[(r_S), p_{\text{corr}}]$ .

	$\text{H}\alpha$ FWHM ( $r_S$ )	$\text{H}\beta$ FWHM ( $r_S$ )	$\text{MgII}$ FWHM ( $r_S$ )
$\text{H}\beta$ FWHM	(0.8) 99		
$\text{MgII}$ FWHM	(0.8) 75	(0.4) 72	
$\text{CIII]}$ FWHM	(—) —	(—) —	(0.2) 13

Percentages are not given where there were fewer than 7 data pairs.

correlation between  $L_{\text{H}\alpha}$  and  $L_{0.2\text{keV}}$ .

Given that the intrinsic spectrum of AGN is expected to peak in the largely unmeasurable EUV (which provides much of the ionizing photon flux), the luminosity at 0.2 keV should be most closely related to the strength of the broad emission lines (except perhaps for MgII which is produced by 0.6-0.8 keV photons; Krolik & Kallman 1988), yet all of the lines have the weakest dependence on  $L_{0.2\text{keV}}$  (i.e. compared to  $L_{5000}$ ,  $L_{2500}$  and  $L_{2\text{keV}}$ ). In Paper I we suggested that the RIXOS AGN sample has a large proportion of moderately absorbed AGN with column densities of the order of  $10^{21} \text{ cm}^{-2}$ . Columns of this size will greatly modify  $L_{0.2\text{keV}}$  but will have a much lesser effect on the optical/UV lines and continuum. Since our measurement of  $L_{0.2\text{keV}}$  has not been corrected for any intrinsic absorption, we would not

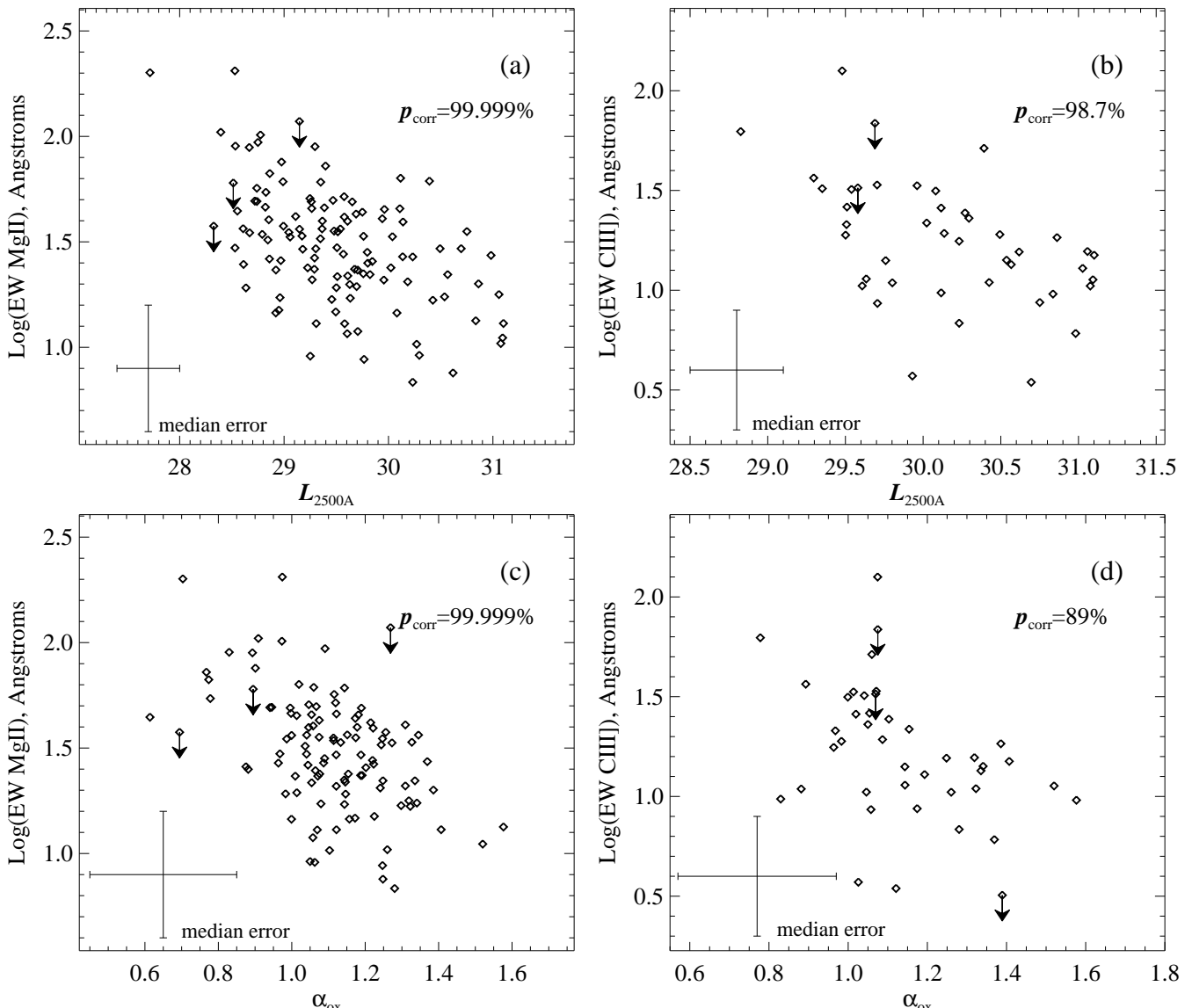


**Figure 4.** An illustration of the Baldwin effect in MgII and CIII]. Arrows indicate upper limits on the line EWs. (a) MgII EW plotted against  $L_{2500}$ , and (b) CIII] EW plotted against  $L_{2500}$ . There are also correlations with  $\alpha_{\text{ox}}$ ; (c) MgII EW plotted against  $\alpha_{\text{ox}}$ , (d) CIII] EW plotted against  $\alpha_{\text{ox}}$ .

then expect it to be a reliable indicator of the strength of the local ionizing flux and thus the observed line and 0.2 keV luminosities would tend not to be related.

While there is only a weak dependence of the H $\alpha$  luminosity on  $L_{2\text{keV}}$ , there is a strong correlation between the EW of H $\alpha$  and  $L_{2\text{keV}}$ , suggesting a relationship between the strength of H $\alpha$  relative to the local optical continuum, and the strength of the hard X-ray power-law. The MgII and CIII] EWs are anti-correlated with the local UV continuum luminosity (i.e.  $L_{2500}$ ); this is the ‘Baldwin effect’ (see Figure 4a-b and Section 4.3). There are also anti-correlations between the MgII and CIII] EWs and  $\alpha_{\text{ox}}$  (Fig 4c-d); these may be induced by the strong  $L_{2500}$  versus  $\alpha_{\text{ox}}$  correlation for those objects, however since the measurements of  $\alpha_{\text{ox}}$  have additional scatter (see Section 4), a primary correlation between the MgII and CIII] EWs and  $\alpha_{\text{ox}}$  is also possible.

## 4.2 Line-line correlations

All of the line luminosities are strongly correlated with each other (the correlation between  $L_{\text{H}\alpha}$  and  $L_{\text{MgII}}$  is relatively weak but is calculated from only 7 data pairs). In Table 4a, it can be seen that for the H $\alpha$ , H $\beta$  and [OIII] lines, their EWs are strongly correlated with their own luminosities. This is discussed further in Section 4.3 which addresses the evidence for Baldwin effects in the RIXOS AGN emission lines.

### 4.2.1 FWHM-EW correlations

Relationships between the FWHM and EW of AGN emission lines have been reported previously; a correlation has been observed in H $\beta$  (Osterbrock 1977; Gaskell 1985; Osterbrock & Pogge 1985; Goodrich 1989; we also find a  $p_{\text{corr}}=99.8$  per cent correlation in the radio-quiet quasars from the BG sample) while anti-correlations are seen in Ly $\alpha$

and  $\text{CIV}\lambda 1549$  (Francis et al. 1992; Wills et al. 1993). In the case of  $\text{H}\beta$ , Gaskell (1985) suggested that this is evidence for radiative acceleration of the line-emitting clouds; the EWs are low because the cloud density is high ( $\log(\text{Ne}) > 10 \text{ cm}^{-3}$ ; this suppresses Balmer line emission) and the cloud velocity is low because the denser clouds experience a weaker radiative acceleration. Osterbrock & Pogge (1985) suggested instead that the lower-velocity Balmer line regions have a smaller covering factor.

For  $\text{Ly}\alpha$  and  $\text{CIV}\lambda 1549$ , Francis et al. (1992) and Wills et al. (1993) demonstrated that the anti-correlation is due to the dominance of a changing core component relative to invariant underlying wings. As the core component grows, the EW increases while the FWHM falls. Two models have been proposed to explain this; (1) a two phase region of the BLR, i.e. a ‘very broad line region’ which emits the broad base of the lines and an ‘intermediate width emission-line region’ from where the line core originates (Francis et al. 1992; Wills et al. 1993); and (2) a ‘bipolar’ model for the BLR where HILs come from a bipolar outflow and LILs from a disc-shaped region (Wills et al. 1993; although this latter model is intended to apply to radio-loud objects which have a well-defined axis).

For the RIXOS AGN, we find a strong *correlation* between the EW and the FWHM of  $\text{MgII}$  (see Fig 5a), i.e. in the same sense as that seen in the low-ionization Balmer lines. A weak (90 per cent) correlation in  $\text{MgII}$  was also seen by B94. There is no evidence for any relationship between the FWHM and EW of  $\text{CIII]$  in the RIXOS AGN; neither was any found by B94. We find a weak (94 per cent) correlation between the FWHM and EW of  $\text{H}\alpha$ , although none was seen in  $\text{H}\beta$ . The lack of a correlation for  $\text{H}\beta$  may be due to a poor determination of the intrinsic  $\text{H}\beta$  parameters, again possibly influenced by the effects of absorption (see also Section 4.5).

#### 4.2.2 Other line-line correlations

For  $\text{MgII}$ , in addition to the FWHM-EW relationship, there is also a weaker (96 per cent) correlation between the FWHM and the line luminosity, thus it is conceivable that these dependences may have been induced by the improper subtraction of underlying  $\text{FeII}$  (see Section 2.2.1). However, there is *no* relationship between the luminosity (or the flux) of the  $\text{MgII}$  line and its EW; there is also a large degree of scatter in the  $L_{\text{MgII}}$ -FWHM correlation (see Fig 5b). Neither does the luminosity-FWHM dependence seem to be related to the Baldwin effect in  $\text{MgII}$ ; there is no correlation between the  $\text{MgII}$  FWHM and  $L_{2500}$ . Rather it implies that when the line is broad, it is strong with respect to the local continuum and its luminosity tends to be high; firm conclusions can only be drawn from higher signal-to-noise spectra however.

B94 have reported an anti-correlation between the  $\text{MgII}/\text{CIII}$  flux ratio and  $\text{CIII}$  FWHM in their sample of 85 quasars, but none between the  $\text{MgII}/\text{CIII}$  flux ratio and  $\text{MgII}$  FWHM. For the RIXOS AGN, we find the opposite, i.e. a strong *correlation* between the  $\text{MgII}/\text{CIII}$  flux ratio and  $\text{MgII}$  FWHM but none for  $\text{CIII}$  FWHM. Using the B94 data, we find that the correlation between the  $\text{MgII}/\text{CIII}$  flux ratio and  $\text{CIII}$  FWHM is very strong in the radio-loud objects but not seen in the radio-quiet AGN. Since we expect

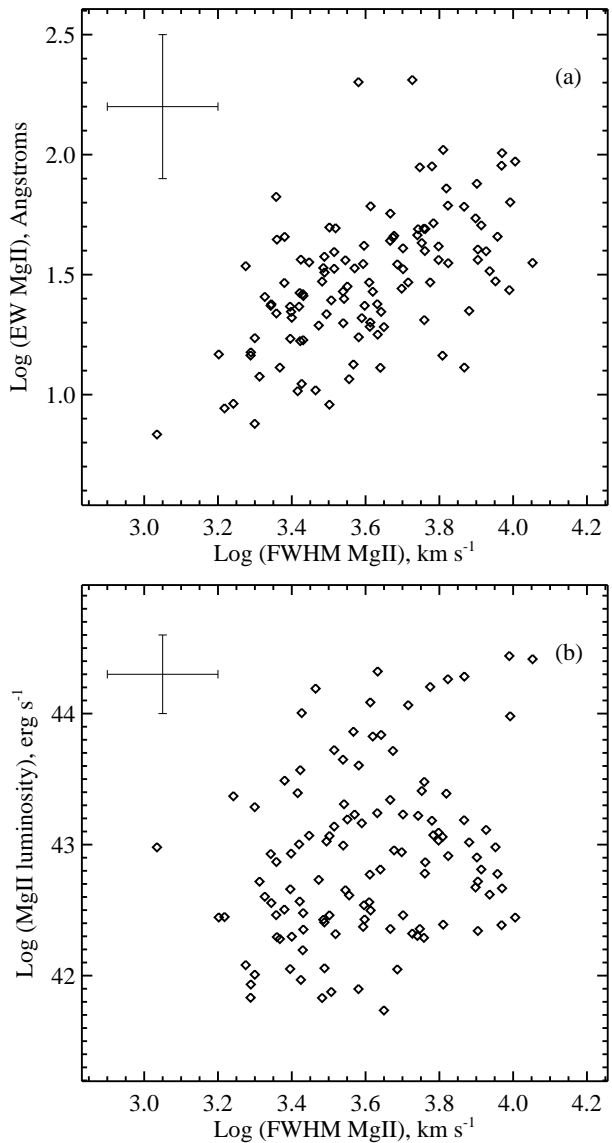


**Figure 5.** The relationships between the  $\text{MgII}$  parameters; (a) EW plotted as a function of FWHM; (b) luminosity plotted against FWHM. Typical error bars are also shown on the plots.

that the RIXOS AGN are predominantly radio-quiet, this may account for the discrepancy between the two samples for  $\text{MgII}/\text{CIII}$  versus  $\text{CIII}$  FWHM. The correlation between this flux ratio and the  $\text{MgII}$  FWHM in the RIXOS AGN may be induced by the dependence of  $L_{\text{MgII}}$  on  $\text{MgII}$  FWHM.

#### 4.3 The Baldwin effect

The ‘Baldwin effect’ is a term describing the anti-correlation of a line’s EW with the continuum luminosity and was originally discovered in  $\text{CIV}\lambda 1549$  (Baldwin 1977). We find evidence of a Baldwin effect in  $\text{MgII}$  and  $\text{CIII}$  (with  $p_{\text{corr}} > 99.9$  per cent and 99.3 per cent respectively; see Figure 4a and b). SS91 also found Baldwin effects in  $\text{MgII}$  and  $\text{CIII}$ ; in both lines the effect was stronger in the radio-loud subsample (i.e. when compared to radio-quiet). There is no evidence of a Baldwin effect in the optical lines of the RIXOS AGN (i.e.  $\text{H}\alpha$ ,  $\text{H}\beta$  and  $[\text{OIII}]$ ).

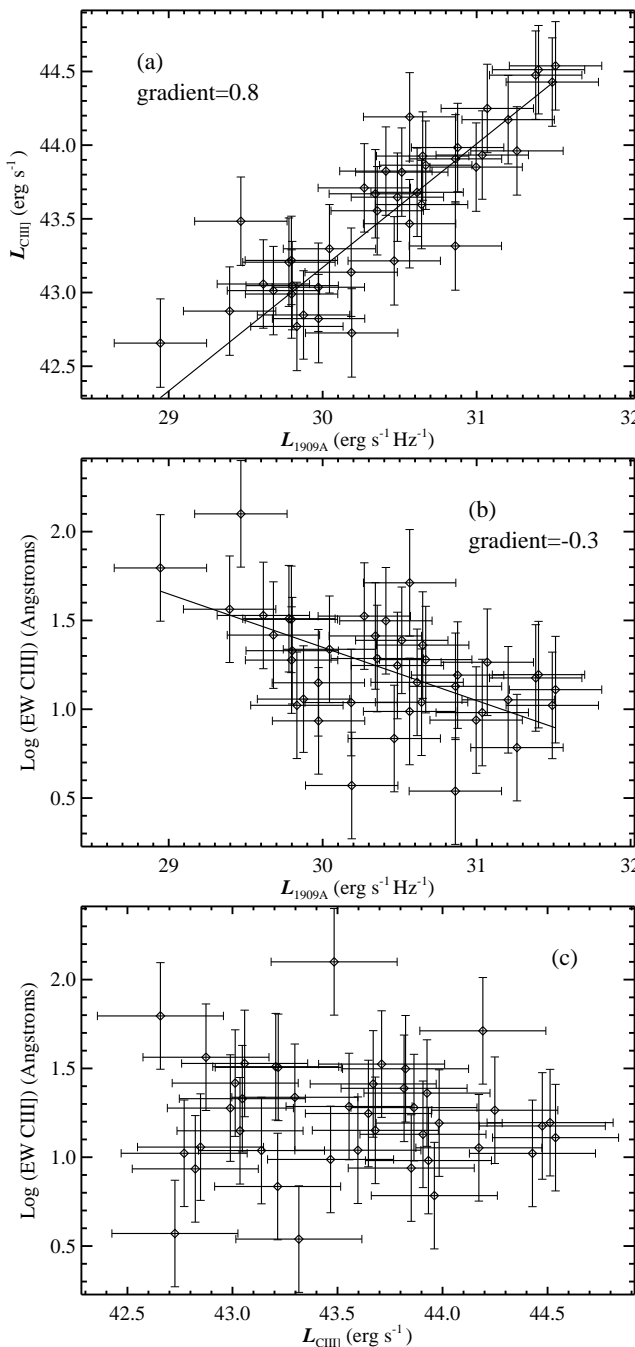


**Figure 6.** A demonstration of the Baldwin effect in CIII]. (a) CIII] line luminosity is plotted as a function of the continuum luminosity at the line centre (i.e. at 1909 Å;  $L_{1909\text{A}}$ ). (b) EW plotted against the 1909 Å continuum luminosity; this is the Baldwin effect. (c) The CIII] EW plotted against its own luminosity - there is no significant correlation between these two parameters.

One might expect that the effects of absorption would reduce any Baldwin effects in a sample, because while the UV continuum luminosity (i.e.  $L_{2500}$ ) would be reduced by any dust absorption, the EWs would remain unchanged. However, for a typical column density expected for the RIXOS AGN ( $\sim 10^{21} \text{ cm}^{-2}$ ; Paper I), the difference in  $L_{2500}$  is only  $\sim 0.4$  dex (for a Galactic dust-to-gas ratio), which is small compared to the scatter on the data (see Fig 4a).

Therefore, it would not be unreasonable to expect the Baldwin effect to remain significant in a sample of moderately absorbed AGN such as this.

The Baldwin effect arises because there is a tight correlation between the luminosity of an emission line and the luminosity of its local continuum. We can demonstrate this by fitting a linear slope to the line versus continuum luminosity data (in log-log space) and using the gradient as a measure of the relative rate of change in the line luminosity. For example in Fig 6a,  $L_{\text{CIII]}}$  is plotted as a function of the continuum at the position of CIII] (i.e. at 1909 Å). A straight line fitted to these data (taking into account the errors) gives a gradient of  $0.8 \pm 0.1$ , i.e. the line luminosity increases more slowly than the continuum, so a plot of EW (the ratio of the line to continuum luminosities) versus continuum data should show an anti-correlation with a gradient of  $\sim -0.2$ . Indeed the log(CIII] EW) versus continuum data are strongly anti-correlated; a straight line fitted to the data has a gradient of  $-0.3 \pm 0.1$  (Fig 6b). Note in Fig 6c, the lack of a significant correlation between the CIII] EW and the CIII] luminosity.

Repeating this for H $\alpha$ , we calculate a gradient of  $1.3 \pm 0.3$  for the  $L_{\text{H}\alpha}$  versus H $\alpha$  continuum data, i.e. the H $\alpha$  luminosity increases faster than the local continuum. In this case we might expect a correlation between the H $\alpha$  EW and the continuum (i.e. an ‘inverse’ Baldwin effect) but none is actually seen. However, there is a strong correlation between the H $\alpha$  EW and the H $\alpha$  luminosity which suggests that the line luminosity (rather than the continuum) has the strongest influence on the behaviour of the EW. A similar situation occurs for H $\beta$  and [OIII], i.e. although inverse Baldwin effects might be expected, the line EWs are correlated with the line luminosity rather than the continuum.

The Baldwin effect must be possible because the strength of the continuum local to the line is closely related to that part of the continuum which produces the line emission. The photons primarily responsible for producing H $\alpha$  and H $\beta$  lie in the 13.6-54.4 eV and 0.3-0.8 keV ranges, for CIII] the Lyman continuum (13.6-24.5 eV) is most important, while MgII requires photons with energies between 0.6-0.8 keV (Krolik & Kallman 1988). Thus the detection of Baldwin effects in CIII] and MgII suggests that the UV continuum is strongly related to the EUV and soft X-rays, while the lack of Baldwin effects in the optical lines implies that the optical continuum is less so. This is to be expected since the UV and soft X-ray continua are probably dominated by the same component, i.e. the big blue bump (BBB; Walter & Fink 1993; Laor et al. 1994, 1997; Fiore et al. 1995; Paper I), while emission from the host galaxy (and perhaps an optical power-law component) becomes more significant at longer wavelengths, so that the optical continuum at  $\lambda \geq 5000$  Å is less likely to be as strongly related to the strength of the BBB.

We can measure the direct response of one of the emission lines given in this paper to its ionizing continuum; MgII is produced primarily by 0.6-0.8 keV photons which fall within the range of the PSPC data. A straight-line fitted to a plot of  $L_{\text{MgII}}$  versus the 0.7 keV luminosity (calculated from the best-fitting power-law models to the X-ray data) has a slope of  $1.2 \pm 0.1$  i.e. the line luminosity increases faster than that of its ionizing continuum, but more slowly than its local continuum. This could be due to the effects of absorp-

tion, removing more of the ionizing continuum flux than the MgII flux. However, for a Galactic dust-to-gas ratio and assuming the dereddening curves of Cardelli et al. (1989), we find that the dust removes more light at 2800 Å [60 per cent for an E(B-V) of 0.17] than an ‘equivalent’ column of cold gas removes at 0.7 keV (40 per cent for  $N_{\text{H}}=10^{21} \text{ cm}^{-2}$ ). It may be that the dust-to-gas ratio is lower than the Galactic value in the RIXOS AGN, or this may indicate a non-linear relationship between the strength of MgII and its soft X-ray ionizing continuum. Measurements of  $L_{\text{MgII}}$  and the 0.7 keV luminosity in a sample of unabsorbed AGN would provide clearer evidence of this.

#### 4.4 Balmer decrement

If absorption does have a major influence on properties of the sample, i.e. hardening  $\alpha_x$  and softening  $\alpha_{\text{opt}}$ , then one might also expect to see its effects on other parameters, for example on the Balmer decrement (as measured by the  $\text{H}\alpha/\text{H}\beta$  flux ratio). If it can be assumed that the case B recombination value for the Balmer decrement always applies, then the *intrinsic* ratio will be  $\sim 3$ . Any dust extinction along the line of sight will preferentially absorb the optical spectrum at shorter wavelengths, thus the Balmer decrement increases with the amount of dust.

The Balmer decrements are plotted as a function of the X-ray spectral index,  $\alpha_x$ , in Fig 7. There is no formal correlation between these parameters using the Spearman test, although the mean Balmer decrement for the RIXOS AGN is  $5 \pm 1$  ( $1\sigma$  standard deviation; neglecting uncertain values for  $\text{H}\beta$ ), suggesting some degree of dust absorption present in the sample. Using the reddening curve of Cardelli et al. (1989) and assuming a Galactic dust to gas ratio, we find a typical  $N_{\text{H}}$  from the RIXOS AGN Balmer decrements of  $\sim 0 - 2 \times 10^{21} \text{ cm}^{-2}$  (i.e. for those AGN with both  $\text{H}\alpha$  and  $\text{H}\beta$  measurements; 23 objects). This is consistent with the continuum modelling of Paper I, where we found column densities up to  $\sim 3 \times 10^{21} \text{ cm}^{-2}$ .

#### 4.5 Continuum slopes

##### 4.5.1 Balmer line FWHM

The relationships between Balmer line FWHM and optical/UV and X-ray slopes are plotted in Fig 8. The object with the broadest FWHM which lies away from the main distributions is source number 6 in field 273 (i.e. F273-006), a radio-quiet AGN with double-peaked Balmer lines (Puchnarewicz, Mason & Carrera 1996b). The incidence of double-peaked line emission is very rare in radio-quiet AGN and may indicate that the nature of this object is quite different from the general population, e.g. it may contain two BLRs each orbiting its own supermassive black hole in a binary system, or the line emission may be formed in opposing jets or radiation cones.

##### 4.5.2 X-ray spectral slope and Balmer line FWHM

Although strong relationships between the  $\text{H}\beta$  FWHM and the soft X-ray spectrum have been observed in other samples of AGN, we have found no similar dependence in the RIXOS AGN (Fig 8a). Puchnarewicz et al. (1992) found a tendency for ultra-soft X-ray AGN to have narrow Balmer

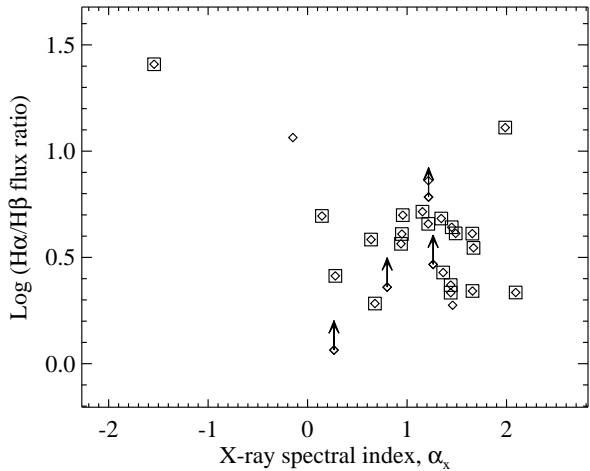


**Figure 7.** Balmer decrement (i.e.  $\text{H}\alpha/\text{H}\beta$  flux ratio) for the RIXOS AGN plotted as a function of X-ray spectral index,  $\alpha_x$ . All AGN, including those with uncertain measurements of the  $\text{H}\beta$  line, are plotted as diamonds. Boxes are drawn around the more secure measurements of  $\text{H}\beta$ , while the arrows indicate those objects with upper limits on the  $\text{H}\beta$  flux.

lines, while Laor et al. (1994, 1997) reported a strong anti-correlation between  $\alpha_x$  and the FWHM of  $\text{H}\beta$  for their sample of PG quasars (although they reported none for  $\text{H}\alpha$ ). Boller, Brandt & Fink (1996; hereafter BBF) showed that narrow-line Seyfert 1s (NLS1s; Seyfert galaxies whose permitted lines are broader than the forbidden lines, yet have FWHM of less than  $2000 \text{ km s}^{-1}$ ; Osterbrock & Pogge 1985) tend to have soft X-ray spectral slopes. They also demonstrated that there seem to be no AGN with both broad  $\text{H}\beta$  FWHM and soft 0.2-2 keV spectra.

We combine the Laor et al. (1997) and BBF results on  $\text{H}\beta$  with the RIXOS AGN in Fig 9. All of the measured FWHM for the RIXOS sample, including ‘uncertain’ values for the FWHM, are shown. The RIXOS data extend to harder values of  $\alpha_x$  but are largely consistent with the BBF sample at softer slopes,  $\alpha_x \gtrsim 1$ . The Laor et al. data are consistent with both samples. Together, these data seem to confirm a lack of lines with broad FWHM at soft  $\alpha_x$ , rather than a true anti-correlation between the two quantities. Note that none of the RIXOS AGN which have an  $\alpha_x$  harder than 0.5 (where presumably the absorption is greatest) also had a well-defined  $\text{H}\beta$  line. These objects tend to have weak  $\text{H}\beta$  lines whose broad components are difficult to discern. An intrinsic anti-correlation in  $\text{H}\beta$  may thus be diluted by the effects of absorption, which suppress the broad component of the  $\text{H}\beta$  line, artificially narrowing the overall profile (this assumes that the absorption only affects the broad line component of the emission lines and not the narrow component).

Searching for an anti-correlation between  $\alpha_x$  and the Balmer line FWHM in absorbed AGN may best be made using  $\text{H}\alpha$  rather than  $\text{H}\beta$ , as this is the stronger line and is modified less by dust. This is demonstrated particularly well by F278-010, a  $z=0.09$  Seyfert 1.9 ( $\alpha_x=-1.5 \pm 0.3$ ) which is plotted in Fig 10. The  $\text{H}\alpha$  line is well-defined and its broad component has a FWHM of  $7100 \text{ km s}^{-1}$ , while only the narrow component of  $\text{H}\beta$  can be seen, presumably because this object suffers from strong dust absorption which has removed the broad  $\text{H}\beta$  emission. This may happen to a lesser

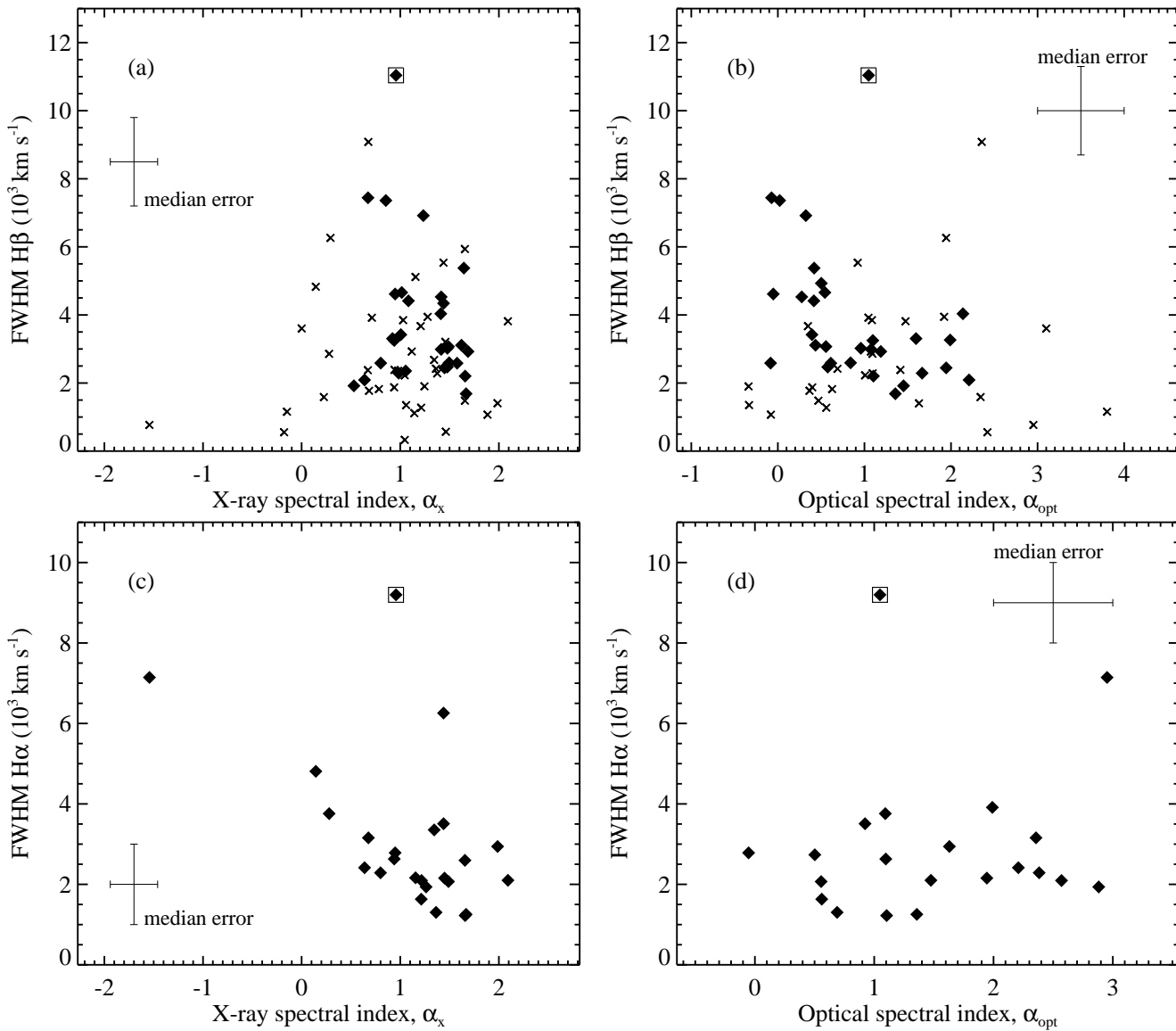


**Figure 8.** Balmer line width plotted as a function of the X-ray spectral index,  $\alpha_x$ , and optical index,  $\alpha_{\text{opt}}$ . Good data are plotted as diamonds while AGN with uncertain  $H\beta$  FWHM are drawn as crosses. A box is drawn around source F273\_006 (RX J1042+1212) which exhibits unusually broad, double-peaked Balmer line emission. (a)  $H\beta$  FWHM versus  $\alpha_x$ , (b)  $H\beta$  FWHM versus  $\alpha_{\text{opt}}$ , (c)  $H\alpha$  FWHM versus  $\alpha_x$  and (d)  $H\alpha$  FWHM versus  $\alpha_{\text{opt}}$ .

degree in AGN with intermediate values of  $\alpha_x$ , artificially narrowing the  $H\beta$  line and thus masking a true correlation.

There is some indication ( $p_{\text{corr}}=91$  per cent) of an anti-correlation between the FWHM of  $H\alpha$  and the X-ray spectral index,  $\alpha_x$  (in the sense that objects with narrow lines have softer X-ray spectra and vice-versa; see Fig 8c). This is in the same sense as the correlation between  $H\beta$  FWHM and  $\alpha_x$  seen in AGN with soft X-ray spectra by Laor et al. (1994,1997). Removing the three outliers with  $\alpha_x < -0.5$  and  $H\alpha$  FWHM  $< 5500 \text{ km s}^{-1}$ , reduces  $p_{\text{corr}}$  to 83 percent, while remaining visually suggestive of an anti-correlation. Recalling that the slope of the X-ray spectrum in the RIXOS AGN is thought to be a mean indicator of the level of the absorption, an inverse dependence of  $H\alpha$  FWHM on  $\alpha_x$  would then suggest that when the absorption is low, so that we have an unobscured line of sight to the nucleus (and  $\alpha_x$  is

soft), the velocity of the Balmer-line emitting region is relatively low, and rises as the absorption increases.

Absorption in the BBF and Laor et al. (1997) samples is unlikely to be the cause of this apparent dependence however, as these AGN generally have a much softer  $\alpha_x$  and suffer less from the effects of absorption. The relationship between  $H\beta$  FWHM and  $\alpha_x$  seen in the BBF and Laor et al. samples is more likely to be related to the *intrinsic* strength of the soft X-ray component (see e.g. BBF for a review); the differences between these and the RIXOS sample are discussed in more detail in Section 5.6.1.

#### 4.5.3 Optical slope and Balmer line FWHM

We find a strong correlation ( $p_{\text{corr}}=99$  per cent) between the  $H\beta$  FWHM and the slope of the optical continuum,

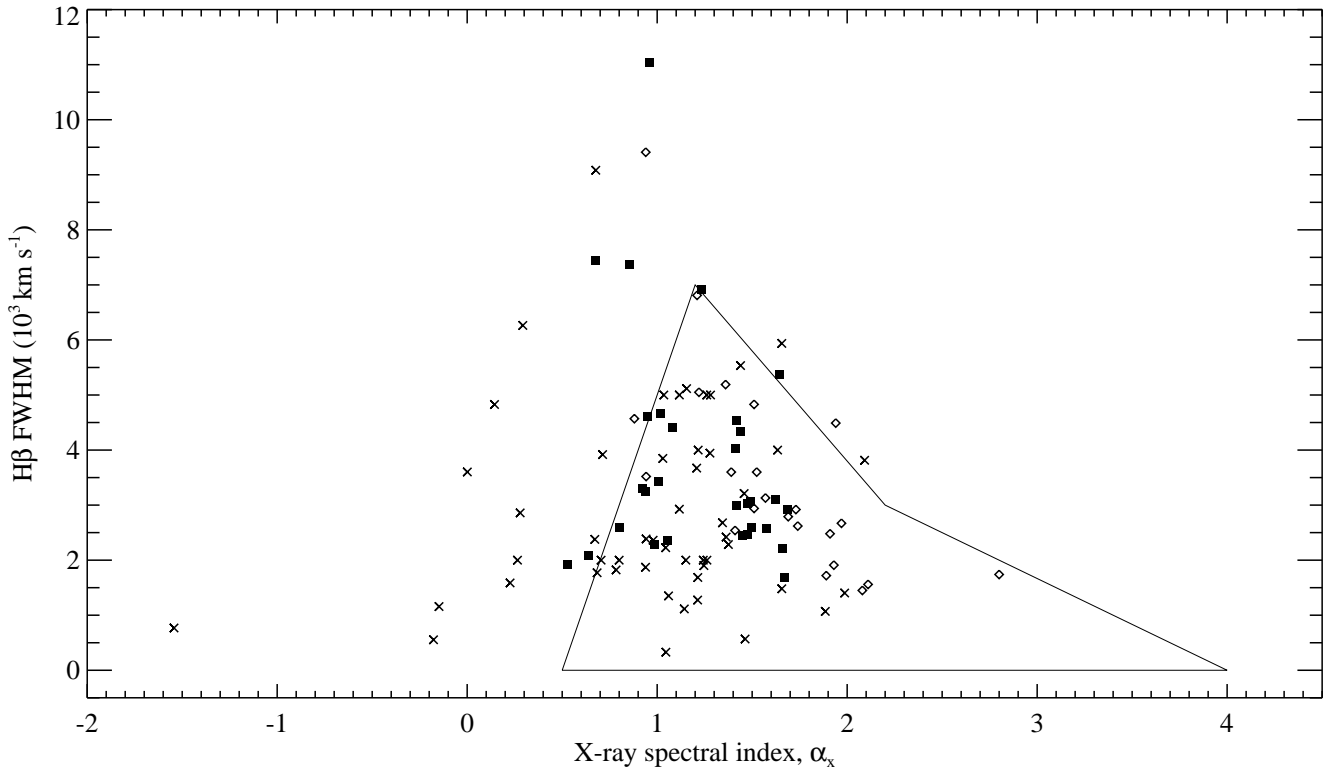


**Figure 9.**  $H\beta$  FWHM plotted as a function of the X-ray spectral index,  $\alpha_x$ , for the RIXOS (solid squares), Laor et al. (1997; diamonds) and BBF (region enclosed by thin line). RIXOS AGN where the uncertainties on the  $H\beta$  FWHM are relatively high, are plotted as crosses.

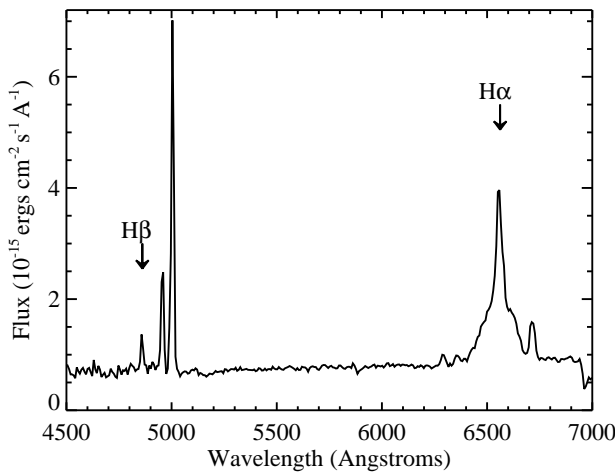


**Figure 10.** The optical spectrum of F278-010, a  $z=0.09$  Seyfert 1.9 galaxy, plotted in the rest-frame of the AGN. Note the very broad  $H\alpha$  line and the lack of a broad  $H\beta$  component.

in the sense that AGN with harder optical/UV spectra have broader line widths, and vice-versa. However, when we combine the  $H\beta$  FWHM and  $\alpha_{\text{opt}}$  values from other samples with the RIXOS AGN, the correlation disappears: see Fig 11 where we compare the RIXOS data with the Laor et al. (1997) and Puchnarewicz et al. (1992) samples.

In the optical/UV part of the spectrum, the continuum slope softens (reddens) as the amount of absorption increases, thus in a situation analogous to that for  $\alpha_x$ , the

FWHM of the broad  $H\beta$  components will be most difficult to measure in sources with the softest  $\alpha_{\text{opt}}$ . This selection effect is reflected in Fig. 11, which shows an overall lack of broad  $H\beta$  lines when  $\alpha_{\text{opt}}$  is soft. On the strength of the data shown in Fig 11, we conclude that there is probably no dependence between  $H\beta$  FWHM and  $\alpha_{\text{opt}}$  in AGN in general.

#### 4.5.4 Other line correlations with continuum slope

There are weak ( $p_{\text{corr}}=98$  per cent) anti-correlations between the  $H\beta$  and  $[\text{OIII}]$  luminosities and the slope of the optical continuum ( $\alpha_{\text{opt}}$ ), although these may be induced by the  $p_{\text{corr}}>99.995$  per cent correlation between  $\alpha_{\text{opt}}$  and  $L_{2500}$  ( $L_{2500}$  is also strongly correlated with  $L_{H\beta}$  and  $L_{[\text{OIII}]}$ ).

The  $\text{MgII}$  luminosity shows a correlation with  $\alpha_{\text{os}}$  and a weaker dependence on  $\alpha_{\text{ox}}$ , although these may be induced by strong correlations ( $>99.995$  per cent) between  $L_{2500}$  and  $\alpha_{\text{os}}$  and between  $L_{2500}$  and  $\alpha_{\text{ox}}$  for AGN with measured  $\text{MgII}$  emission. This is also true for  $L_{[\text{CIII}]}$ . The  $\text{MgII}$  EW is strongly anti-correlated with  $\alpha_{\text{ox}}$ ; see Section 4.1.

## 5 DISCUSSION

Understanding the production of emission lines in AGN is a complex task and many different factors must be taken into account, including the physical conditions and geometry of the line-emitting gas (e.g. density, temperature, opacity, distance from the ionizing source, distribution of the gas), the nature of the incident continuum (e.g. intensity, spectral

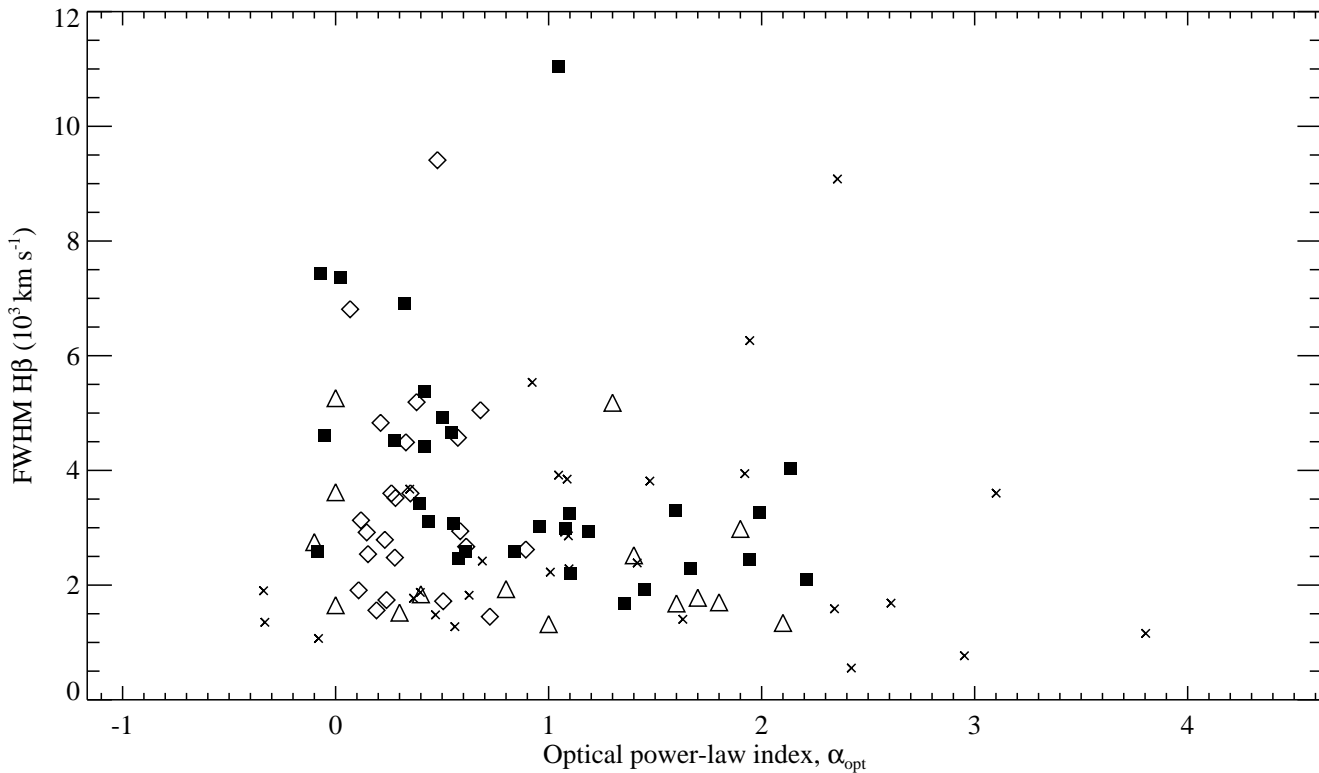


**Figure 11.** H $\beta$  FWHM plotted as a function of the optical power-law index,  $\alpha_{\text{opt}}$ , for the RIXOS, Laor et al. (1997) and Puchnarewicz et al. (1992; i.e. the Ultra-Soft Survey, or 'USS' AGN) samples. The RIXOS AGN are drawn as solid squares, the Laor et al. quasars as diamonds and the USS AGN are plotted as triangles. RIXOS AGN with poor measurements of the H $\beta$  FWHM are plotted as crosses.

shape and degree of anisotropy) and the effects of possible orientation-dependence in any assumed AGN model.

### 5.1 The RIXOS sample

When considering the properties of the RIXOS AGN in the context of BLR models, the exact nature of the sample must be taken into account. The RIXOS AGN are X-ray selected and drawn from medium-deep ( $>8$  ksec) observations made with the *ROSAT* PSPC, so with this sample we are probing the relatively faint X-ray emitting population, i.e. AGN with an observed flux of  $>3 \times 10^{-14}$  erg s $^{-1}$  (between 0.4 and 2.4 keV). The use of the *ROSAT* 'hard' band (i.e. above 0.4 keV) means that the sample is insensitive to the properties of any soft X-ray excess (which dominates at lower energies, e.g. Pravdo et al. 1981; Arnaud et al. 1985; Turner & Pounds 1989; Puchnarewicz et al. 1992). One consequence of this is that the mean  $\alpha_x$  for the RIXOS AGN ( $\alpha_x = 1.07 \pm 0.63$ ; Mittaz et al. 1997) is significantly harder than that of samples selected using softer X-rays (e.g. for Walter & Fink 1993, the mean  $\alpha_x$  is  $1.50 \pm 0.48$ ) or by UV-excess methods (for the Laor et al. 1997 sample of PG quasars, the mean  $\alpha_x$  is  $1.63 \pm 0.07$ ). Another is that AGN whose PSPC spectra are dominated by a very soft X-ray excess (see e.g. Puchnarewicz et al. 1995; BBF) have been selected against in the RIXOS AGN sample.

By ignoring the spectrum below 0.4 keV, this sample can also encompass AGN with moderate amounts of intrinsic absorption by cold gas (i.e. with column densities,  $N_{\text{H}}$ , of a few times  $10^{21}$  cm $^{-2}$ ). In Paper I, where we considered

the properties of the optical/UV and X-ray continua of the RIXOS AGN, we concluded that this is a sample of objects whose intrinsic spectra are absorbed by cold gas and dust with  $N_{\text{H}}$  in the range 0 to  $\sim 3 \times 10^{21}$  cm $^{-2}$ . This is an important result because it implies that for the sample overall, correlations between the optical/UV and X-ray parameters may not necessarily be indicative of intrinsic dependences but rather a reflection of the level of absorption by dust in the optical/UV and by cold gas in the soft X-rays.

In the following discussion, we assess the results presented in this paper in the context of present models for the physical nature of the BLR, bearing in mind the significance of possible absorption by gas and dust and its effect on observed correlations.

### 5.2 Models of BLR geometry

Recently, significant progress in characterizing the geometry of the BLR has been made with the reverberation-mapping of the BLRs in nearby Seyferts (see e.g. Peterson 1993 and references therein). This technique has prompted many changes to the original 'standard' model of the BLR (Davidson & Netzer 1979; Kwan & Krolik 1981), where cold line-emitting clouds are pressure confined by a hot, inter-cloud medium and HILs and LILs are emitted from different parts of the same cloud. Some of the latest models, which are based on the intensive NGC 5548 monitoring campaign (Clavel et al. 1991; Peterson et al. 1991), suggest that the HIL and LIL are emitted from spatially distinct regions; an inner, roughly spherical high-ionization zone and an outer,

flattened low-ionization zone (Krolik et al. 1991; O'Brien, Goad & Gondhalekar 1994).

Other models include those of Wills et al. (1993) who proposed two possible geometries largely based on FWHM-EW correlations (see Section 4.2.1). The first is the existence of an ‘intermediate width emission-line region’ (ILR) and a ‘very broad line region’ (VBLR) in addition to the usual NLR; the ILR is effectively a higher velocity ( $\sim 2000 \text{ km s}^{-1}$ ), higher density extension of the NLR. A similar ‘transition line region’ was suggested by van Groningen & de Bruyn (1989) based on asymmetries and broad components in the H $\beta$  and [OIII] lines of bright Seyfert 1 nuclei (see also Mason, Puchnarewicz & Jones 1996). The VBLR has a high density, lies closer to the central black hole and has velocities of  $\sim 7000 \text{ km s}^{-1}$ . It emits a relatively invariant broad component while the ILR produces a more dynamic ‘core’; differences in the relative proportions of these features cause the observed correlations. The second Wills et al. (1993) model, the ‘bipolar’ model (more appropriate for radio-loud AGN), invokes HILs from a bipolar outflow while the LILs come from a flattened ensemble of dense clouds; in this case the correlations are a consequence of orientation effects.

### 5.3 Emission line strengths

Beginning with the strengths of the optical and UV emission lines, we now examine the overall properties of the RIXOS AGN with respect to models of AGN geometry, and taking into account the possible effects of absorption.

In Sections 3.1 and 3.2, we found that the strengths of the Balmer lines (luminosities and EWs) are low relative to optically-selected AGN, whereas the EWs of [OIII] are comparable with optically-selected samples. The EWs of CIII] and MgII are also typical of other AGN (see Section 3.3). We consider whether these results may be explained in a geometry similar to the ‘unified model’ of AGN (e.g. Antonucci 1993), a cross-section through which is illustrated in Figure 12.

#### 5.3.1 Broad line region

The broad line regions (including the HIL and broad Balmer line region) lie within the molecular torus. If they are seen at viewing angles which pass through the torus, the line and continuum luminosities will be reduced by the same factor, so that the EWs should remain unchanged relative to face-on orientations (this assumes that the optical/UV continuum is also emitted from within the torus, and that the line and continuum emission is isotropic). While this appears to be true for the UV lines (whose EWs are ‘normal’ compared to other AGN), the Balmer lines have relatively low EWs: this implies that the Balmer line fluxes are intrinsically weak.

The reason for this may be systematic differences in the shape of the ionizing continuum incident on the BLR between X-ray and non-X-ray selected AGN. An important point is that the photons most directly linked to the production of CIII] and MgII are different from those for H $\alpha$  and H $\beta$  (Krolik & Kallman 1988; see also Section 4.3). CIII] responds to relatively low energy EUV photons (13.6-24.5 eV) and MgII to soft X-rays (600-800 eV). The Balmer lines also respond to these energies, but also to photons which reach further into the EUV at low and high energies (i.e. up to

54.4 eV and also from 300-600 eV), i.e. they will be more sensitive to the relative peak flux of the big bump component. Thus if the big bumps are relatively weak in X-ray selected AGN, then the H $\alpha$  and H $\beta$  lines will also be weak, but CIII] and MgII could be less strongly affected.

#### 5.3.2 Narrow line region

While NLR-type gas clouds may completely surround the torus, only those which lie in the cone of ionizing light defined by the torus will emit the narrow lines observed (see Fig 12). Furthermore, because the NLR is probably greatly extended relative to the torus, our viewing angle to the NLR is expected to have little effect on the observed narrow line flux (but see Baker 1997 for evidence of possible anisotropies in [OIII] emission). Thus when an AGN is observed at viewing angles which pass through the torus, the optical continuum will be low but the [OIII] emission should be unaffected, and NLR EWs in absorbed AGN should be relatively high compared to unobscured samples. Based on absorption columns for the RIXOS AGN derived from the modelling in Paper I, we estimate that the mean [OIII] EW for this sample should be twice that of an unabsorbed sample of AGN (Section 3.2). However the EWs of the RIXOS AGN are typical of optically-selected objects. This may be because the [OIII] ionizing flux is also relatively low for the RIXOS AGN as discussed in Section 5.3.1. The observed [OIII] EWs would then be reduced, effectively counteracting the effects of absorption by the torus.

### 5.4 Emission line response to the continuum

The presence of Baldwin effects in CIII] and MgII show (a) that the UV continuum luminosity is related to the EUV/soft X-ray luminosities (i.e. the ionizing continua of these lines); and (b) that the luminosities in both lines increase more slowly than that of their *local* (UV) continua. Several mechanisms have been proposed as the cause of the Baldwin effect; the following assume dependences on luminosity, e.g. as the luminosity increases then either (1) the ionization parameter (which describes the number of available ionizing photons per atom or ion) decreases (Mushotzky & Ferland 1984); (2) the shape of the ionizing continuum softens (Schultz 1982; Zheng & Malkan 1993); or (3) the BLR cloud density decreases (Rees, Netzer & Ferland 1989). Also, Shields, Ferland & Peterson (1995) proposed that the non-linear response of the emission lines to the continuum flux is due to a mixture of optically-thick and -thin clouds in the BLR.

Although the actual ionizing continuum of CIII] lies in the EUV and thus cannot be measured directly, the ionizing continuum of MgII, which lies between 0.6-0.8 keV, has been observed for the RIXOS AGN, so that we are able to determine the response of the MgII to changes in its ionizing flux. A linear fit to a plot of  $L_{\text{MgII}}$  versus 0.7 keV luminosity indicates that the luminosity of the line is increasing faster than its ionizing continuum. This favours models which propose changes in the physical conditions of the line-emitting gas, rather than changes in the continuum shape (and a linear line response) for the cause of the Baldwin effect, at least in MgII.

We could find no evidence of a Baldwin effect in the Balmer lines or [OIII] (see Section 4.4), suggesting that the

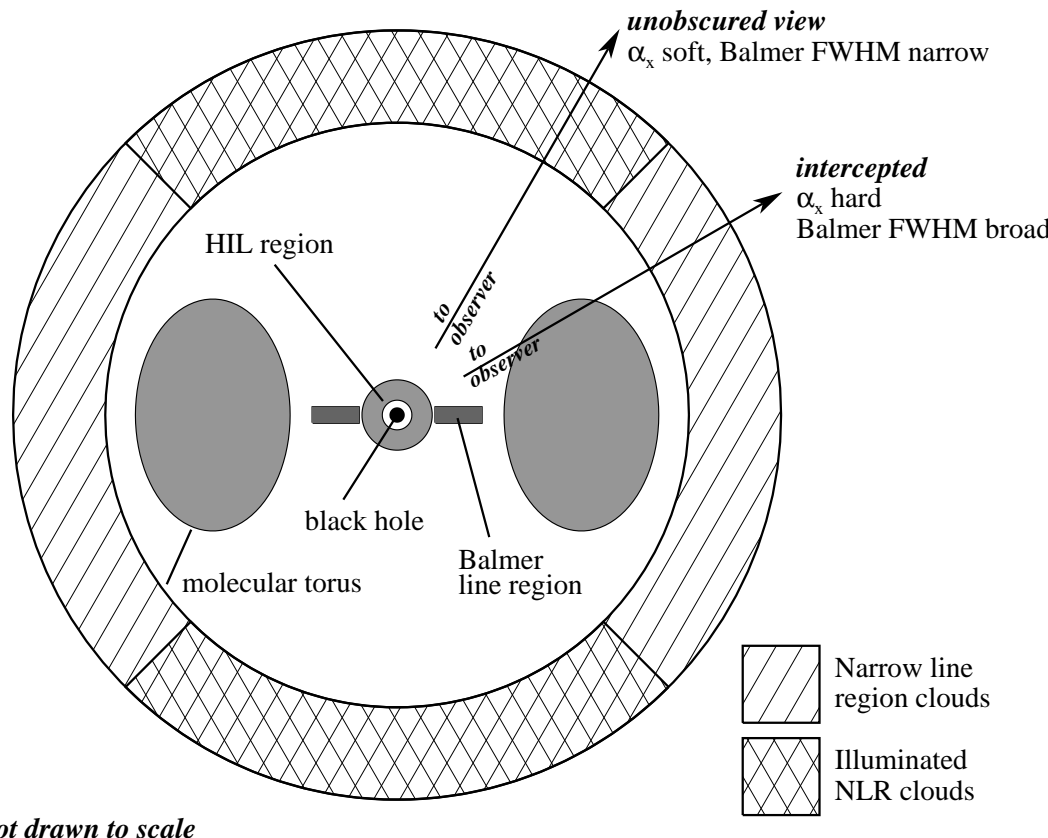


**Figure 12.** A cross-section through an AGN and an illustration of the possible orientation-dependence in the emission properties. The BLR is made up of an inner spherical HIL region (which emits CIII] and MgII), and an outer flattened LIL zone which emits the broad Balmer lines. While the NLR may completely surround the inner regions, if the molecular torus is optically-thick, then only clouds which do not lie in the shadow of the torus will be illuminated by the nucleus. When an AGN is viewed at angles close to face-on so that the nucleus is unobscured,  $\alpha_x$  is soft and the broad components of the Balmer lines are narrow. As the viewing angle increases, the soft X-rays are absorbed, hardening  $\alpha_x$ , while the line-of-sight velocity of the Balmer line-emitting regions increases (i.e. the FWHM increase). CIII] and MgII, which are emitted from the spherical HIL region, show no dependence of FWHM on  $\alpha_x$ .

luminosity in the EUV/soft X-ray regions is not strongly correlated with the optical continuum (i.e. at  $\lambda \gtrsim 5000 \text{ \AA}$ ). This may be due to the effects of galactic contamination which are more significant at longer wavelengths. With the UV line responses, these results are consistent with the presence of a single component which dominates throughout the optical/UV to soft X-rays and we identify that component with the big bump.

### 5.5 FWHM-EW correlations

Evidence regarding the structure of the BLR may be found from relationships between the EWs and FWHM of the emission lines. For example, in the RIXOS AGN we find strong evidence ( $p_{\text{corr}} > 99$  per cent) for a correlation between the FWHM and EW of MgII. Reports of similar correlations for H $\beta$  have also been made, while anti-correlations have been observed in Ly $\alpha$  and CIV $\lambda 1549$  (see Section 4.2.1). Thus while relationships between FWHM and EW seem to be typical of several different emission lines, the actual nature of the relationship depends on whether the lines are of

a high- or low-ionization species, i.e. in general there is an anti-correlation in the HILs and a correlation in the LILs.

In the case of the HILs, Wills et al. (1993) proposed that the emission lines have two components, one relatively constant component from the VBLR, and a more dynamic 'core' from the ILR (a similar model was proposed by Francis et al. 1992). Essentially, as the core increases relative to the broad underlying component, the EW increases but the line becomes narrower at half maximum, leading to the observed anti-correlation. The LILs generally have lower velocities than the HILs, thus they are more likely to dominate in the ILR. However, an opposite dependence is seen in the LILs [H $\alpha$ , MgII (this paper; see Section 4.2.1) and H $\beta$  (Osterbrock 1977; Gaskell 1985; Osterbrock & Pogge 1985; Goodrich 1989)]; this suggests an intrinsic correlation between the EW and FWHM of lines emitted from the ILR.

Thus the implications of the various FWHM-EW correlations in the context of the VBLR/ILR model suggest (1) that the HIL emission originates mostly from the VBLR with an additional component from the ILR; (2) that the LIL emission is emitted mostly from the ILR; (3) that the VBLR

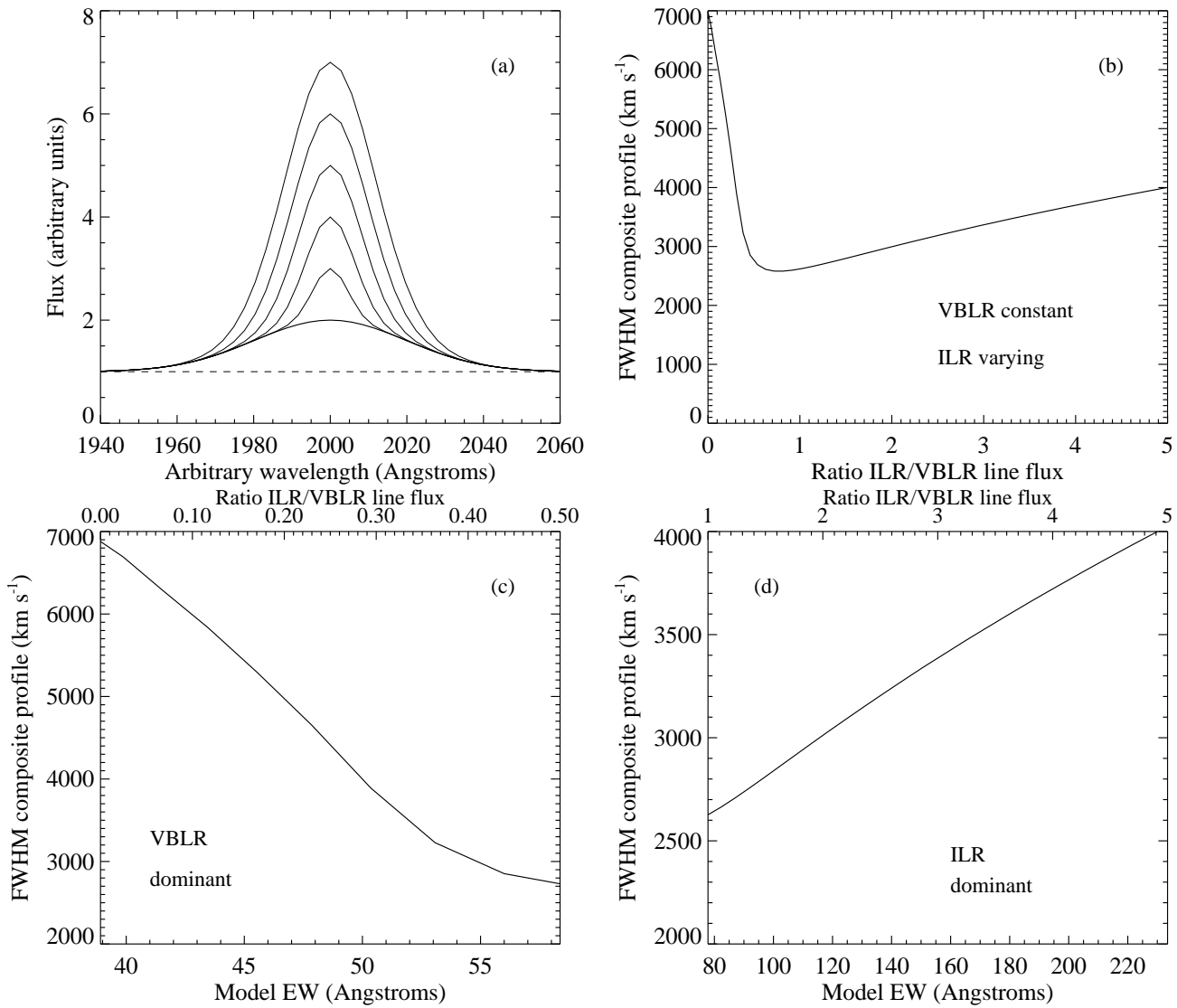


**Figure 13.** A model of the emission line profiles for a two-component VBLR plus ILR representation of a typical AGN emission line. The model assumes a constant VBLR component and a varying contribution from the ILR. (a) Predicted line profiles for an arbitrary line, where the ILR peak flux varies from 0 to five times that of the VBLR component. The continuum is drawn as a dashed line, the profile with zero ILR flux as a thick, solid line and profiles with increasing ILR contributions as thin solid lines. (b) The model FWHM over the full range of ILR/VBLR ratio (i.e. where the peak flux in the ILR component is varied from 0 to 10 times that of the peak VBLR flux). (c) A close-up view at low ILR/VBLR flux ratios, predicting an anti-correlation between FWHM and EW in observed data when the VBLR dominates. (d) At high ILR/VBLR flux ratios, the intrinsic dependence of ILR FWHM on the ILR line strength dominates and a correlation is observed between FWHM and EW.

component is relatively invariant and shows no dependence between the FWHM and EW; and (4) that the ILR component is much more dynamic and exhibits an intrinsic correlation between the velocity of the gas which comprises it and the strength of the lines it emits (i.e. the lines are narrow when their EW is low).

To test whether such a scheme can reproduce the observed dependences in the HILs and LILs, we have constructed a simple model of an emission line which is made up of two components (i.e. from an ILR and a VBLR), and measured the FWHM and EW as the relative contribution of each changes. Each individual component is represented

by a Gaussian. The VBLR component has a FWHM of  $7000 \text{ km s}^{-1}$  and its peak flux is constant. The peak flux in the ILR component varies from 0 to 10 times that of the VBLR; its FWHM increases linearly with the peak flux, from  $1000 \text{ km s}^{-1}$  to  $4000 \text{ km s}^{-1}$ , i.e. in this model we are assuming an intrinsic correlation between the strength and the FWHM of a line in the ILR. A composite model profile is constructed over a range of ILR to VBLR flux ratios and the FWHM and total flux are measured for each.

The resulting FWHM of the composite profile as a function of the ILR to VBLR flux ratio is shown in Fig 13b (the model FWHM is plotted as a function of EW in Fig

13c-d; for a constant continuum flux, the EW is linearly dependent on the ILR/VBLR flux ratio). When the VBLR flux is strong, the changing relative contribution from the ILR component dominates the change in profile and an anti-correlation is observed. Then as the ILR flux increases, the VBLR component is less important and the underlying correlation between the line strength and its FWHM is dominant. Thus this model can simultaneously satisfy the FWHM-EW dependences observed in  $\text{CIV}\lambda 1549$ ,  $\text{Ly}\alpha$ ,  $\text{MgII}$  and the Balmer lines.

### 5.5.1 Line strength and velocity in the ILR

The correlation between the EW and FWHM of  $\text{H}\beta$  was suggested by Gaskell (1985) to be due to radiative acceleration of the line-emitting clouds. For this model, AGN with weak and narrow Balmer lines have relatively high density LIL clouds. It decouples line FWHM from its dependence on the angle of the line of sight, and argues against orientation as the cause of the FWHM- $\alpha_x$  correlations. However, intermediate-dispersion spectroscopy of the narrow-line Seyfert 1 galaxy RE J1034+396 suggests that, for this AGN at least, it is more likely that the low-velocity line-emitting gas has a relatively low, rather than high, density, when compared with more typical AGN (Mason et al. 1996).

Alternatively, Osterbrock & Pogge (1985) proposed that the dependence of  $\text{H}\beta$  FWHM on EW may be due to a smaller cloud covering factor (i.e. leading to a lower line flux) when the lines have low velocity. A low-velocity, weakly-emitting LIL region could be a consequence of a more distant outer BLR which also has a smaller covering factor. Such a model supports a relationship between the relative position of the outer LIL regions and the amount of cold absorbing gas which lies beyond, i.e. that the amount of cold gas is high when the covering factor of the LIL region is high, and the LIL regions lie closer to the centre.

For the orientation-dependent model, a simple explanation for an increase in line EW as the viewing angle increases, is if the line emission is anisotropic and beamed back towards the central ionizing source. If the LIL region is disc-shaped, then the lines will be emitted preferentially along the plane of the disc, so that as the viewing angle increases, both the FWHM and EW (assuming the continuum to be relatively isotropic) would also increase, leading to the observed correlation.

### 5.5.2 Location of the $\text{CIII}$ emission

The  $\text{CIII}\lambda 1909$  line is only emitted at relatively low densities ( $\log(\text{Ne}) < 9.5 \text{ cm}^{-3}$ ), yet it is generally very broad; indeed the  $\text{CIII}$  line tends to be broader than  $\text{CIV}\lambda 1549$ , e.g. in the B94 sample, the mean  $\text{CIII}$  to  $\text{CIV}\lambda 1549$  FWHM ratio is 1.2. This suggests (1) that any  $\text{CIII}$  emission from the ILR is relatively weak (since this has low velocity); and (2) that it is emitted from regions closer to the black hole than  $\text{CIV}\lambda 1549$ .

Although Krolik et al. (1991) concluded that  $\text{CIII}$  could not be emitted from the same region as other HILs, O'Brien et al. (1994) found that it was possible if they allowed for negative responsivity in the BLR (i.e. where the emissivity of a line decreases with increasing ionization parameter). They proposed that the ionization parameter decreases with

radius throughout the HIL region and that the inner parts (where the ionization parameter is high) are probably optically thin at the Lyman limit, permitting  $\text{CIII}$  emission from the HIL region. If  $\text{CIII}$  is emitted from the inner regions of the HIL region, this might explain why its FWHM is generally broader than that of  $\text{CIV}\lambda 1549$ , despite its lower state of ionization and its low critical density.

No relationship has been found between the FWHM and EW of  $\text{CIII}$ ; neither was any found in the  $\text{CIII}$  data of B94. This suggests that there is no intrinsic FWHM-EW relationship in the VBLR (i.e. similar to that which is inferred for the ILR).

## 5.6 FWHM and the X-ray spectral slope

### 5.6.1 Balmer lines

A tendency for the  $\text{H}\beta$  line to be narrow when  $\alpha_x$  is soft has been seen in other samples of AGN (Puchnarewicz et al. 1992; Laor et al. 1994, 1997; BBF), yet none is seen in the RIXOS sample. However, the RIXOS AGN are probably absorbed in the optical/UV and soft X-rays, so that their  $\text{H}\beta$  lines may be significantly modified by dust absorption in many cases (Section 4.5.2). This would mean that their FWHM are no longer a reliable indicator of the intrinsic velocity of the broad Balmer line regions. The  $\text{H}\alpha$  line, which is stronger and less affected by dust than  $\text{H}\beta$ , should provide a more accurate measurement of the velocity of the Balmer line regions in dust-absorbed AGN. Indeed we find that the FWHM of  $\text{H}\alpha$  does tend to be narrow when the X-ray spectrum is soft, and vice-versa, i.e. in the same sense as that seen for  $\text{H}\beta$  in the unabsorbed AGN.

Thus the  $\text{H}\alpha$  FWHM- $\alpha_x$  dependence in the RIXOS AGN seems to extend the relationship between Balmer line width and soft X-ray slope to much harder X-ray slopes (see Fig. 8c), to  $\alpha_x \sim 0$  and possibly as low as  $\alpha_x = -2.0$  (although only one data point falls below  $\alpha_x = 0$ , it does extrapolate from the distribution at softer  $\alpha_x$ ). However the underlying physical reason for the trends seen in the comparison samples may be different to that seen in the RIXOS AGN; the Puchnarewicz et al. (1992) and BBF samples are both dominated by AGN with very soft X-ray spectra while the Laor et al. objects are bright, PG quasars which have relatively strong UV excesses and a mean  $\alpha_x$  of  $\sim 1.6$ : these objects are expected to suffer little intrinsic absorption and their values of  $\alpha_x$  are thus more likely to reflect the intrinsic strength of the soft X-ray excess. In addition, their  $\text{H}\beta$  profiles should be relatively unobscured, so that the  $\text{H}\beta$  FWHM versus  $\alpha_x$  correlation suggests an intrinsic link between the soft X-ray component and the ‘true’ Balmer line velocity.

For the RIXOS AGN, we have argued that the range in  $\alpha_x$  reflects the degree of cold gas absorption (Paper 1) and not the changing strength of the soft component. In other words, despite a change in the physical interpretation of the slope of the soft X-ray spectrum, the correlation between the soft X-ray slope and the velocity of the Balmer line regions appears to remain. Any plausible model for this relationship must incorporate this change.

### 5.6.2 UV lines

There are no correlations between the UV line FWHM and the soft X-ray slope. Since the  $\text{CIII}$  and  $\text{MgII}$  lines are generally dominated by the broad component and strong enough,

despite any absorption, to permit a reliable measurement of their FWHM, this probably reflects a ‘real’ lack of dependence. It suggests that the regions where CIII] and MgII dominate are different from those which emit the Balmer lines.

### 5.7 Orientation dependence

A dependence of Balmer line width on the X-ray spectral slope for the RIXOS AGN implies that the Balmer line-emitting regions ‘know’ the amount of cold gas which surrounds them. This may be either because the soft X-ray slope has a direct, physical influence on the Balmer line gas, or because the soft X-ray slope and Balmer line velocity both depend on a third parameter.

A ‘third parameter’ upon which Balmer line width and  $\alpha_x$  (or equivalently for the RIXOS AGN, the amount of absorption) may both depend, is the orientation of the nucleus itself to our line of sight. Previous studies have shown that the Balmer lines may be emitted from a flattened, possibly disc-shaped region. If it can be assumed that the Balmer line clouds are circulating in the disc and that the FWHM are dominated by their velocity along the line of sight, then the lines will be narrow when our line of sight is perpendicular to the disc (i.e. when the disc is seen face-on), and they will broaden as the viewing angle increases (the viewing angle is defined to be the angle between the line of sight and the axis of the disc). With regard to  $\alpha_x$ , in Paper I we showed that the cold gas and dust absorption may arise in the molecular torus which lies beyond the BLR. When our viewing angle to the molecular torus is small (i.e. more face-on), any nuclear soft X-ray emission will have a clear line of sight to the observer; as the viewing angle increases, more of the torus’ material will intervene, hardening  $\alpha_x$ . Therefore, if the Balmer line region lies in the same plane as the molecular torus, then as the viewing angle increases, the Balmer line FWHM will increase and  $\alpha_x$  will harden, producing the correlation observed (this is illustrated in Fig 12). A similar geometry was proposed by Baker (1997), who suggested that absorption by dust between the BLR and NLR is due to orientation dependence, and that this is the cause of the correlation between radio core dominance and optical luminosity in radio-loud AGN.

A continuation of this model to much softer AGN is possible if the strength of the unabsorbed soft X-ray component is also related to the viewing angle. This is possible for the accretion disc model, if the inner edge of the disc is puffed-up so that it is geometrically-thick (e.g. Czerny & Elvis 1987; Madau 1988). In this case the soft X-rays are emitted in a cone-shaped region along the axis of the disc so that the disc spectrum shifts to lower energies (and thus out of the soft X-ray band) as the viewing angle increases. Therefore if the disc is co-planar with the Balmer line regions and the molecular torus, then it is possible that the Balmer line FWHM versus  $\alpha_x$  correlation may continue from ultrasoft AGN to those like the absorbed RIXOS sources.

#### 5.7.1 Dust absorption and the [OIII] EW

The significance of orientation effects on quasar emission line properties was studied by BG and Boroson (1992), using a sample of 81 (mostly radio-quiet) UV-excess objects from

the Bright Quasar Survey (Schmidt & Green 1983). It had already been suggested that the optical continuum in *radio-loud* quasars is intrinsically anisotropic; i.e. that it is brighter when the nucleus is viewed face-on (Browne & Wright 1985; Jackson et al. 1989; Baker 1997). Studies of the permitted lines in radio-loud quasars have indicated that their line FWHM may also be orientation-dependent, i.e. narrower when observed face-on (Miley & Miller 1979; Boroson & Oke 1984; Wills & Browne 1986). Boroson (1992) tested the hypothesis that the optical continuum and line emission in *radio-quiet* quasars is similarly anisotropic by searching, at fixed  $L_{[OIII]}$ , for a correlation between H $\beta$  FWHM and [OIII] EW (the latter will be angular-dependent if  $L_{[OIII]}$  is isotropic and the optical continuum is *anisotropic*). No correlation was found, and Boroson (1992) concluded that this type of orientation effect may *not* be significant in the general quasar population, or at least, not in objects with UV excesses.

We are unable to perform a similar test with the RIXOS AGN, because of the effects of dust absorption; this modifies the observed strength of the nuclear optical continuum (which is supposed to indicate the inclination angle), and removes the broad H $\beta$  component so that the H $\beta$  FWHM can not be used to ‘measure’ the intrinsic Balmer line region velocity. Furthermore, the [OIII] EW will itself be affected by dust absorption (sections 3.2 and 5.3), so although we cannot reproduce the Boroson (1992) test, we are able to make a further test for the position of the absorbing medium using  $\alpha_{opt}$  and the [OIII] EW. If the dust does lie between the source of the optical continuum and the [OIII] region, then the [OIII] EW should increase as  $\alpha_{opt}$  softens. No dependence is seen however (see Table 3), although since the optical continuum around 5000 Å may contain significant emission from the host galaxy, the overall effect may be diluted. If instead we look at the dependence of the  $L_{[OIII]}/L_{2500}$  ratio on  $\alpha_{opt}$ , (at 2500 Å, any galactic emission is weak and the effects of dust absorption are greater), we do find a strong correlation ( $p_{corr}=98$  per cent for objects where the rest-frame 2500 Å flux has been measured directly, see Fig 14;  $p_{corr}=99$  per cent when extrapolated values of  $L_{2500}$  are included). This is consistent with effects of dust absorption and suggests that the dust does indeed lie between the BLR and the NLR.

#### 5.7.2 UV line emission

The CIII] lines are often thought to be produced in the HIL region which, in the Krolik et al. (1991) and O’Brien et al. (1994) models, are roughly spherical. This means that their FWHM would not be expected to reflect any changes in viewing angle; if, for the RIXOS AGN,  $\alpha_x$  is an indicator of the viewing angle, then the lack of a FWHM- $\alpha_x$  dependence in CIII] is consistent with a spherical CIII]-region in the orientation-dependent model.

The lack of a FWHM- $\alpha_x$  correlation for MgII implies that this line may also be emitted from a spherical region (in the orientation model), rather than a flattened, disc-like geometry which has been suggested for other LILs. Also, the mean FWHM of MgII is low relative to CIII] (Section 3.3), indicating that it is emitted from regions which lie further out from the black hole than CIII] (assuming that the cloud velocities reflect the gravitational potential of the black hole;

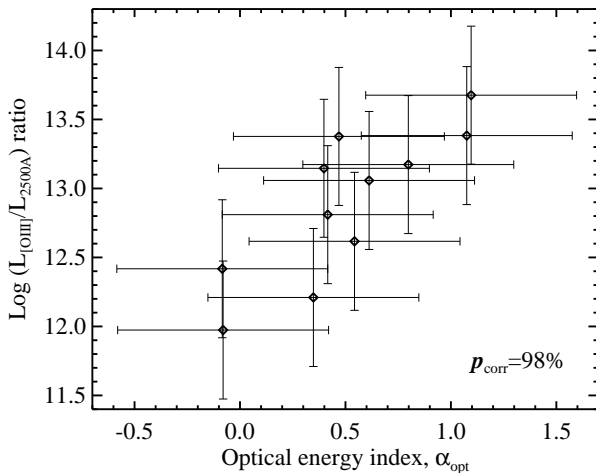


**Figure 14.** The correlation between the  $L_{[\text{OIII}]}/L_{2500}$  ratio and the slope of the optical continuum,  $\alpha_{\text{opt}}$ . The data shown are only for those AGN where  $L_{[\text{OIII}]}$  and  $L_{2500}$  have been measured directly.

see e.g. Krolik et al. 1991).

We note that in the Wills et al. model where the HILs are emitted primarily from a paraxial flow, while a second, flattened emission line region produces the LILs, an orientation dependence in the CIII] and MgII emission would be seen. Since no such dependence is implied for the RIXOS AGN, this model is probably inappropriate for this sample.

### 5.8 Low intrinsic velocity

Rather than an orientation dependence, the observed emission line FWHM may reflect intrinsic differences in the velocity of the line-emitting regions, for example the lines may be narrow because (a) the line region lies further out from the central black hole, and/or (b) the mass of the black hole is relatively small so that, if the cloud velocity is Keplerian in nature, the orbital velocities are low (see e.g. Laor et al. 1994, 1997; BBF). For unobscured AGN, where  $\alpha_x$  reflects the strength and/or the temperature of the soft X-ray component, this would imply a direct relationship between  $\alpha_x$  and FWHM, e.g. when  $\alpha_x$  is soft, the BLR may be physically pushed-out or extended. Alternatively, the BLR may simply be ‘lit-up’ at greater distances due to a ‘fine-tuning’ of the necessary conditions (i.e. ionization parameter and density) for line emission (see e.g. Baldwin et al. 1996).

These physical interpretations suggest that the Balmer line regions are responding directly to the shape of the soft X-ray spectrum. In this case, a correlation would only be seen if the observer saw the same spectrum as that ‘seen’ by the Balmer line clouds. However for the RIXOS AGN, if the absorption does occur *beyond* the BLR (as suggested here and in Paper I) then no correlation should be seen (since the intrinsic slope of the soft X-ray spectrum is not known and  $\alpha_x$  now reflects the amount of absorption). Yet the H $\alpha$  FWHM does appear to be dependent on  $\alpha_x$ , although the weakness of the formal correlation ( $p_{\text{corr}}=91$  per cent) may indicate that the relationship is beginning to break down as  $\alpha_x$  hardens. If a dependence of H $\alpha$  FWHM on  $\alpha_x$  is confirmed to hard X-ray slopes, then it would imply (for these kinds of models) that the velocity of the outer BLR ‘knows’

the amount of absorbing gas which lies beyond.

The lack of FWHM- $\alpha_x$  correlations for CIII] and MgII would suggest that  $\alpha_x$  has no effect on these line-emitting regions, while there is an observable difference to the broad Balmer line gas (whether this is direct or indirect). Thus any mechanism which operates on the broad Balmer line gas is probably not significant in the regions where CIII] and MgII are produced.

This has implications for the suitability of these kinds of models. Take, for example, the case where the high-velocity Balmer line gas might be removed when  $\alpha_x$  is soft (which leads to relatively narrow Balmer line emission); the mechanism which removes portions of the BLR must be able to destroy the gas very selectively, without also disturbing the CIII] and MgII-producing regions. It is also unlikely that the BLR has been ‘pushed-out’ en masse, since both UV and Balmer line FWHM would then change in response to  $\alpha_x$ . However, it is possible that the Balmer line region has been extended leaving the inner regions unchanged; if the outer (low-velocity) parts of the BLR dominate the Balmer line emission, (see e.g. Rees et al. 1989), then the Balmer line widths could vary independently of the UV line FWHM. In such a situation, it only remains then to explain why the outer BLR extends to much lower velocities when the level of cold gas and dust absorption is low (and vice-versa).

### 5.9 BLR geometry and MgII emission

The behaviour of the MgII line appears to be quite contrary, especially in the context of the orientation-dependent model. Like the Balmer lines, its FWHM is *correlated* with its own EW, suggesting that its ‘broad’ component is emitted from the ILR region (Table 1 shows that ‘very broad’ components are also sometimes seen, and these are probably emitted from the VBLR, but they were disregarded when the correlations were made). However, the MgII FWHM shows no dependence on  $\alpha_x$ ; for the orientation-dependent model, this suggests that its emission region must be different from that of the Balmer lines, e.g. it may have a spherical geometry, like CIII]. These two observed dependences are thus contradictory in the orientation model discussed here, i.e. the FWHM-EW correlation supports a flattened MgII region, whereas the lack of a FWHM- $\alpha_x$  correlation favours a spherical zone.

If instead, the observed FWHM distribution is not due to an angular dependence, some of these restrictions are relaxed. The MgII line may be produced within an ILR which has an intrinsic EW-FWHM dependence, perhaps due to a low covering factor at large distances/low velocities, and no anisotropic properties are required. The lack of a FWHM- $\alpha_x$  correlation for MgII then implies that only the very outer, low-velocity regions of the ILR gas, where the Balmer lines are produced, would be affected by (or respond to) changes in  $\alpha_x$ . This would favour an extension of the outer BLR to lower velocities when  $\alpha_x$  is soft (and absorption is low) and a smaller radial extent of the BLR when  $\alpha_x$  is hard (i.e. the level of absorption is high).

## 6 CONCLUSIONS

Using the AGN identified by the RIXOS survey (Mason et al. , in preparation), we have investigated the optical- and

UV-emission line properties of 160 X-ray selected Seyfert 1s and quasars. Line luminosities, EWs and FWHM of each emission line subsample have been compared with optical/UV and X-ray continuum parameters (slopes and luminosities) and we have looked at the relationships between the lines themselves.

The Balmer lines of the RIXOS AGN are weak relative to optically-selected AGN whereas the [OIII] lines are more typical. This is consistent with the presence of a dust absorber lying between the BLR and the NLR (perhaps in the molecular torus), and a weakened ionizing continuum incident on the Balmer and [OIII]-emitting regions (Sections 3.2 and 5.7.1). The EWs and FWHM of the UV lines (MgII and CIII]) are indistinguishable from those of radio-quiet AGN (which are expected to dominate this sample), implying that their ionizing flux may be comparable to that of optically-selected AGN.

We find Baldwin effects in MgII and CIII], but none in the optical lines. Although MgII increases more slowly than its local continuum, it rises *faster* than its ionizing continuum which lies in the soft X-rays (0.6-0.8 keV). This suggests that, for MgII at least, the Baldwin effect is caused by changes in the physical conditions of the line-emitting gas or on the ionization parameter, as a function of continuum luminosity.

We find a correlation between the FWHM and EW of MgII and discuss this and other FWHM-EW dependences for both high- and low-ionization lines. We extend the VBLR/ILR model (proposed previously to explain anti-correlations between the FWHM and EWs of HILs) to the LIL regions, with the additional premise that there is an intrinsic correlation between FWHM and EW in the ILR. We present a simple demonstration of this model and show that it can predict the various relationships between both HILs and LILs. A relationship between FWHM and EW in the ILR may be due to a reduction in the covering fraction of the LIL regions when its velocity is low, and thus perhaps also when it lies relatively further out from the black hole. This scenario tends to support a link between the amount of cold, dusty gas which lies beyond the BLR and the distance to and covering fraction of the outer BLR, i.e. that when the BLR extends to greater radii from the centre, there is less cold gas beyond.

In the orientation-dependent model, an obvious explanation for the FWHM-EW correlations seen in the LILs would be anisotropic line emission from a disc-shaped LIL region. However the behaviour of the MgII line does not fit easily into this geometry; although there is a correlation between the EW and FWHM of MgII, there is no dependence of MgII FWHM on  $\alpha_x$ , which would be expected in the orientation model if MgII, like the Balmer lines, was also emitted from a disc-like LIL zone.

Although an anti-correlation between H $\beta$  FWHM and  $\alpha_x$  has been seen in unabsorbed samples of AGN, none is observed in the RIXOS sources. This is probably due to population differences between the samples, i.e. the lack of an H $\beta$  FWHM dependence on  $\alpha_x$  in the RIXOS AGN may well be due to the presence of dust which absorbs the broad component, rendering the apparent FWHM an unreliable indicator of the 'true' velocity of the Balmer line-emitting region in dust-absorbed AGN. The evidence for a dependence of H $\alpha$  FWHM on  $\alpha_x$  in the RIXOS AGN, albeit weak, supports

this hypothesis, since the dust absorption has a lesser effect on the broad component of H $\alpha$ , and it is, of course, also the stronger line. An anti-correlation between H $\alpha$  FWHM and  $\alpha_x$  in the RIXOS AGN implies that the Balmer line regions 'know' how much absorbing material lies beyond. This may be due to orientation effects or perhaps because the amount of surrounding gas and dust affects the distance at which the Balmer line regions actually form. The FWHM of the UV lines, i.e. CIII] and MgII, are broader than the Balmer lines and independent of  $\alpha_x$ ; this is consistent with their emission from an inner, spherical region as has been suggested for NGC 5548.

## ACKNOWLEDGMENTS

We thank all in the RIXOS team for their work in obtaining and reducing the data, and we are grateful to Paul O'Brien for his advice. We are also very grateful to the referee, Belinda Wilkes, for her thorough and thoughtful report on this paper, which inspired several improvements. The RIXOS project has received observing time under the International Time Programme offered by the CCI of the Canarian Observatories and has received financial support by the European Commission through the Access to Large-Scale Facilities Activity of the Human Capital and Mobility Programme. This research has made use of data obtained from the UK ROSAT Data Archive Centre at the Department of Physics and Astronomy, University of Leicester (LEDAS) and we would especially like to thank Mike Watson and Steve Sembay for their kind assistance. We also thank the Royal Society for a grant to purchase equipment essential to the RIXOS project. IPF and FCG would like to thank the Consejeria de Educacion Cultura y Deportes del Gobierno de Canarias for financial support.

## REFERENCES

- Alexander T., Netzer H., 1994, MNRAS, 270, 781
- Antonucci R., 1993, Ann. Rev. Astron. Astrophys., 31, 473
- Arnaud K. A., Branduardi-Raymont G., Culhane J. L., Fabian A. C., Hazard C., McGlynn T. A., Shafer R. A., Tennant A. F., Ward M. J., 1985, MNRAS, 217, 105
- Baker J. C., 1997, MNRAS, 286, 23
- Baldwin J. A., 1977, ApJ, 214, 679
- Baldwin J. A., et al. , 1996, ApJ, 461, 664
- Blumethal G. R., Keel W. C., Miller J. S., 1982, ApJ, 257, 499
- Boller Th., Brandt W. N., Fink H., 1996, A&A, 305, 53 (BBF)
- Boroson T. A., 1992, ApJ, 399, L15
- Boroson T. A., Green R. F., 1992, ApJS, 80, 109
- Boroson T. A., Oke J. B., 1984, ApJ, 281, 535
- Brotherton M. S., Wills B. J., Steidel C C., Sargent W. L. W., 1994, ApJ, 423, 131 (B94)
- Browne I. W. A., Wright A. E., 1985, MNRAS, 213, 97
- Cardelli J. A., Clayton G. C., Mathis J. S., 1989, 345, 245
- Clavel J. et al. , 1991, ApJ, 366, 64
- Collin-Souffrin S., Dyson J. E., McDowell J. C., Perry J. J., 1988, MNRAS, 232, 539
- Czerny, B., Elvis, M. 1987, ApJ, 321, 305
- Davidson K., Netzer H., 1979, Rev. Mod. Phys., 51, 715
- Edwards A. C., 1980, MNRAS, 190, 757
- Ferland G. J., 1993, University of Kentucky Department of Physics and Astronomy Internal Report
- Ferland G. J., Netzer H., 1979, ApJ, 229, 274

Ferland G. J., Peterson B. M., Horne K., Welsh W. F., Nahar S. N., 1992, *ApJ*, 387, 95

Fiore F., Elvis M., Siemiginowska A., Wilkes B. J., McDowell J. C., Mathur S., 1995, *ApJ*, 449, 74

Francis P. J., Hewitt P. C., Foltz C. B., Chaffee F. H., 1992, *ApJ*, 398, 476

Gaskell C. M., 1985, *ApJ*, 291, 112

Gioia I. M., Maccacaro T., Schild R. E., Stocke J. T., Liebert J. W., Danziger I. J., Kunth D., Lub J., 1984, *ApJ*, 283, 495

Goodrich R. W., 1989, *ApJ*, 342, 224

Gorenstein P., 1975, *ApJ*, 198, 40

Green P. J., 1996, *ApJ*, 467, 61

Hewitt A., Burbidge G., 1989, *ApJS*, 69, 1

Jackson N., Browne I. W. A., Murphy D. W., Saikia D. J., 1989, *Nature*, 338, 485

Kriss G. A., Canizares C. R., 1982, *ApJ*, 261, 51

Krolik J. H., Kallman T. R., 1988, *ApJ*, 324, 714

Krolik J. H., Horne K., Kallman T. R., Malkan M. A., Edelson R. A., Kriss G. A., 1991, *ApJ*, 371, 541

Kwan J. Y., Krolik J. H., 1981, *ApJ*, 250, 478

Laor A., Fiore F., Elvis, M., Wilkes, B. J., McDowell, J. C., 1994, *ApJ*, 435, 611

Laor A., Fiore F., Elvis, M., Wilkes, B. J., McDowell, J. C., 1997, *ApJ*, 477, 93

Madau, P., 1988, *ApJ*, 327, 116

Mason K. O., Puchnarewicz E. M., Jones, L. R., 1996, *MNRAS*, 283, L26

Miley G. K., Miller J. S., 1979, *ApJ*, 228, L55

Mittaz J. P. D., et al. , 1997, *MNRAS*, submitted

Mushotzky R. F., Done C., Pounds K. A., 1993, *Ann. Rev. Astron. Astrophys.*, 31, 717

Mushotzky R. F., Ferland G. J., 1984, *ApJ*, 278, 558

Netzer H., 1993, *ApJ*, 411, 594

Nicholson K. L., Mittaz J. P. D., Mason K. O., 1997, *MNRAS*, 285, 831

O'Brien P. T., Goad M. R., Gondhalekar P. M., 1994, *MNRAS*, 268, 845

Osterbrock D. E., 1977, *ApJ*, 215, 733

Osterbrock D. E., Pogge R. W., 1985, *ApJ*, 297, 166

Peterson B. M., et al. , 1991, *ApJ*, 368, 119

Peterson B. M., 1993, *PASP*, 105, 247

Pfeffermann, E. et al. , 1986, *Proc. S. P. I. E.*, 733, 519

Pravdo S. H., Nugent J. J., Nousek J. A., Jensen K., Wilson A. S., Becker R. H., 1981, *ApJ*, 251, 501

Puchnarewicz E. M., Mason, K. O., Córdova, F. A., Kartje, J., Branduardi-Raymont, G., Mittaz, J. P. D., Murdin, P. G., Allington-Smith, J., 1992, *MNRAS*, 256, 589

Puchnarewicz E. M., Mason K. O., Romero-Colmenero E., Carrera F. J., Hasinger G., McMahon R., Mittaz J. P. D., Page M. J., Carballo R., 1996a, *MNRAS*, 281, 1243 (Paper I)

Puchnarewicz E. M., Mason K. O., Siemiginowska A., Pounds K. A., 1995, *MNRAS*, 276, 20

Puchnarewicz E. M., Mason K. O. and Carrera F. J., 1996b, *MNRAS*, 283, 1311

Rees M. J., Netzer H., Ferland G. J., 1989, *ApJ*, 347, 640

Ryter C., Cesarsky C. J., Audouze J., 1975, *ApJ*, 198, 103

Schmidt H., Green R. F., *ApJ*, 1983, 269, 352

Schultz H., 1992, in *Physics of Active Galactic Nuclei*, ed W. J. Duschl & S. J. Wagner (Berlin:Springer), 235

Shields J. C., Ferland G. J., Peterson B. M., 1995, *ApJ*, 441, 507

Stark, A. A., Gammie, C. F., Wilson, R. F., Ball, J., Linke, R. A., Heiles, C., Hurwitz, M., 1992, *ApJS*, 79, 77

Steidel C. C., Sargent W. L. W., *ApJ*, 1991, 382, 433 (SS91)

Stephens S. A., 1989, *AJ*, 97, 10

Tananbaum, H., et al. , 1979, *ApJ*, 234, L9

Turner, T. J., Pounds, K. A., 1989, *MNRAS*, 240, 833

van Groningen E., de Bruyn A. G., 1989, *A&A*, 1989, 211, 293

Walter, R., Fink, H. H., 1993, *A& A*, 274, 105

Wills B. J., Brotherton M. S., Fang D., Steidel C. C., Sargent W. L. W., 1993, *ApJ*, 415, 563

Wills B. J., Browne I. W. A., 1986, *ApJ*, 302, 56

Wills B. J., Netzer H., Wills D., 1985, *ApJ*, 288, 94

Zheng W., Malkan M. A., 1993, 415, 517

This paper has been produced using the Royal Astronomical Society/Blackwell Science *T<sub>E</sub>X* macros.